

# Emission spectrum of ionized gas in the Irr galaxy Holmberg II.

O. V. Egorov<sup>1\*</sup>, T. A. Lozinskaya<sup>1†</sup>, A. V. Moiseev<sup>2</sup>

<sup>1</sup> *Lomonosov Moscow State University, Sternberg Astronomical Institute, 13 Universitetskij prospekt, Moscow 119234, Russia*

<sup>2</sup> *Special Astrophysical Observatory, Russian Academy of Sciences, Nizhnii Arkhyz 369167, Russia*

Accepted 2012.... Received 2012...; in original form 2012...

## ABSTRACT

We study the ionized gas spectrum of star forming regions in the Holmberg II galaxy using the optical long-slit spectroscopic observations made at the 6-m telescope of the Special Astrophysical Observatory of the Russian Academy of Sciences (SAO RAS). We estimate the oxygen, nitrogen, sulphur, neon, and argon abundances in individual H II regions and find the average metallicity in the galaxy to be  $Z \simeq 0.1$  or  $0.3 Z_{\odot}$  depending on the estimation method employed. We use these observations combined with the results of our earlier studies of the Irr galaxy IC 10 and BCD galaxy VII Zw 403 to compare the currently most popular methods of gas metallicity estimation in order to select among them the techniques that are most reliable for analysing Irr galaxies. To this end, we use the ‘direct’  $T_e$  method and six empirical and theoretical methods. The results of our observations mostly confirm the conclusions of López-Sánchez et al. (2012) based on the analysis of systematic deviations of metallicity estimates derived by applying different methods to ‘model’ H II regions.

**Key words:** galaxies: individual: Holmberg II – galaxies: irregular – galaxies: ISM – ISM: H II regions – ISM: abundances – techniques: spectroscopic

## 1 INTRODUCTION.

The irregular galaxy Holmberg II (Ho II, DDO 50, UGC4305, PGC 23324, VII Zw 223) currently serves as an ideal target for the study of the entire variety of the phenomena associated with the effect of radiation, stellar winds, and supernovae explosions feedback, which determine the structure, kinematics, and chemical composition of the interstellar medium as well as the process of star formation in Irr galaxies.

This gas-rich, non-interacting, and rigidly rotating galaxy is a member of the M81 group and is located at a distance of  $D = 3.39 \pm 0.20$  Mpc (Karachentsev et al. 2003). It is an Im (i.e., Magellanic-type irregular) galaxy with the parameters  $M_B = -16.71 \pm 0.16$  mag,  $B - V = 0.11 \pm 0.05$ ,  $E(B - V) = 0.032$ , and the inclination angle  $i = 38^\circ$  (Moustakas et al. 2010).

The large-scale structure of the galaxy has been well studied in the optical, radio, IR, UV, and X-ray bands. A total of about 40 giant cavities and slowly expanding H I supershells have been found (see Bagetakos et al. 2011 and references therein). The stellar population of Ho II was thor-

oughly studied using the *Hubble Space Telescope* (HST) data (see, e.g., Weisz et al. 2009 and Cook et al. 2012).

A total of 82 H II regions have been found in the Ho II galaxy (Hodge et al. 1994) and for the sake of homogeneity we use HSK numbers to identify them throughout this paper.

Bright emission nebulae reside mostly in the ‘walls’ of giant HI supershells and are concentrated in several ‘chains’ of complexes of ongoing star formation with the brightest nebulae located in the eastern chain (see Fig. 1 and figures in Hunter et al. 1993 and Karachentsev & Kaisin 2007). Stewart et al. (2000) estimate the ages of these star-forming regions to be between 2.4 and more than 6.3 Myr. The large-scale distribution of the H $\alpha$  emission of ionised gas is consistent with that of FUV emission in the galaxy (see, e.g., fig. 6 of Stewart et al. 2000 and fig. 29 of Weisz et al. 2009). In the eastern chain of the brightest nebulae the brightest emission of heated dust is observed (Walter et al. 2007).

Radio observations of the galaxy (Tonque & Westphal 1995; Braun et al. 2007; Heald et al. 2009) revealed continuum radio emission from the region of bright emission nebulae and, in particular, from the brightest eastern chain. The polarised radio emission is also coincident with this chain (Heald et al. 2009). Tonque & Westphal (1995) identified the synchrotron component of radio emission in the

\* E-mail: egorov@sai.msu.ru

† E-mail: lozinsk36@mail.ru

**Table 1.** Log of observations

Spectrum (PA)	Date	Grism	$\Delta\lambda$ , Å	$\delta\lambda$ , Å	$T_{exp}$ , sec	seeing, arcsec
PA102	31.10/01.11.11	VPHG1200B	3700–5500	5.5	4500	0.9
PA102	01/02.11.11	VPHG1200R	5750–7500	5.5	4800	2.2–2.7
PA187	28/29.03.11	VPHG940@600	3700–8500	6.5	2700	2.2
PA187	31.10/01.11.11	VPHG1200R	3700–5300	5.5	1800	0.9
PA304	22/23.12.11	VPHG940@600	3600–8400	6.5	3600	1.8–2.4
PA347	22/23.12.11	VPHG940@600	3700–8500	6.5	5400	1.6–2.0

eastern chain of bright nebulae, and this led them to suspect that the region may contain supernova remnants.

The main goal of our paper is to perform a detailed study of the emission spectrum and estimate the metallicity of ionised gas in the Ho II galaxy by analysing the spectroscopic observations made at the 6-m telescope of the SAO RAS. We also use the available results of earlier spectroscopic observations of the galaxy made by Lee et al. (2003) and Croxall et al. (2009) combined with *HST* archival imaging data to estimate the metallicity in the same way.

We used the seven currently most popular methods to estimate the oxygen abundance, which determines the metallicity of the interstellar medium. Our aim was to compare different techniques by applying them to the observations of a large number of H II regions in the Holmberg II, IC 10, and VII Zw 403 galaxies in order to choose the optimal method for analysing the metallicity of gas in Irr galaxies.

We also attempted to detect the optical emission from the above mentioned hypothetical supernova remnants using the  $I([\text{S II}])/I(\text{H}\alpha)$  line intensity ratio in the spectrum.

The next sections describe our observations, the data reduction technique, present the results, their discussion, and the main conclusions of this paper.

We defer a comparison of the results of spectroscopic observations with the detailed analysis of the kinematics of ionized and neutral gas and with IR emission of the dust component of the galaxy to our forthcoming paper (Wiebe et al., in preparation).

## 2 OBSERVATIONS AND DATA REDUCTION

The observations were made at the prime focus of the SAO RAS 6-m telescope using the SCORPIO multi-mode focal reducer (Afanasiev & Moiseev 2005) and its new version SCORPIO-2 (Afanasiev & Moiseev 2011). When operated in the long-slit mode, both devices have the same slit size ( $6 \text{ arcmin} \times 1 \text{ arcsec}$ ) with a scale of 0.36 arcsec per pixel. However, with a similar spectral resolution SCORPIO-2 provides a twice larger spectral range: the VPHG940@600 grism covers the wavelength interval spanning from 3700 to 8500 Å, whereas with the SCORPIO we used two grisms VPHG1200B and VPHG1200R for the green and red spectral regions, respectively. The CCDs employed were an EEV 42-40 in the SCORPIO and E2V 42-90 (with the sensitivity peak at redder wavelengths) in the SCORPIO-2.

Table 1 gives the log of observations: for each spectrum designated by the position angle of the spectrograph slit it lists the observing date, grism employed, spectral range  $\Delta\lambda$ ,

spectral resolution  $\delta\lambda$  (estimated by the FWHM of air glow lines), total exposure  $T_{exp}$ , and seeing.

Data reduction was performed in a standard way using the IDL software package developed at the SAO RAS for reducing the long-slit spectroscopic data obtained with the SCORPIO and SCORPIO-2.

To increase the signal-to-noise ratio for weak emission nebulae, we binned spectrograms into 5–6 pixel bins along the slit prior to reduction. The binning size was chosen to make the resulting spatial resolution for a single slit position consistent with the maximum ‘seeing’. To compute the correction for the spectral sensitivity of each grism and convert the spectra to the absolute intensity scale, we observed the spectrophotometric standards Hz 44, Feige 34, and AGK+81d266 immediately after the object at a close zenith distance.

We used single- or two-component Gaussian fitting to measure the integrated fluxes of emission lines. We estimated the errors of the measured fluxes by analysing the synthetic spectra with the given signal-to-noise ratio. In this paper we use only the spectral lines with the signal-to-noise ratios greater than 3.

The error intervals listed in the tables and indicated in the figures below correspond to the  $3\sigma$  confidence level.

## 3 RESULTS OF OBSERVATIONS

Fig. 1 shows the location of six spectrograms taken at four slit positions, designated PA102, PA187, PA304, and PA347 in accordance with their position angles. The two panels of the figure show the  $\text{H}\alpha$  images of the galaxy’s star-forming regions. The upper image was taken with the 2.1-m KPNO telescope within the framework of the SINGS survey (Kennicutt et al. 2003) and the lower image was taken by the *HST* (application number 10522) and adopted from the *Hubble* Legacy Archive<sup>1</sup>.

In the north–south direction the PA187 spectrogram crosses the following H II regions (named according to the catalogue of Hodge et al. 1994): HSK 71, HSK 73, HSK 70 (the nebula surrounding an ultraluminous X-ray source – ULX Holmberg II X-1), HSK 69, and HSK 67. The PA102 slit crosses the H II regions HSK 32, HSK 41, HSK 45, HSK 56, HSK 59, and HSK 73. The PA347 slit covers the western chain of H II regions: HSK 7, HSK 15, HSK 17, HSK 16, HSK 20, and HSK 26. The PA304 spectrogram is least informative, because it crosses faint H II regions HSK 65, HSK 61, HSK 57, HSK 31, and HSK 25.

<sup>1</sup> <http://hla.stsci.edu/>

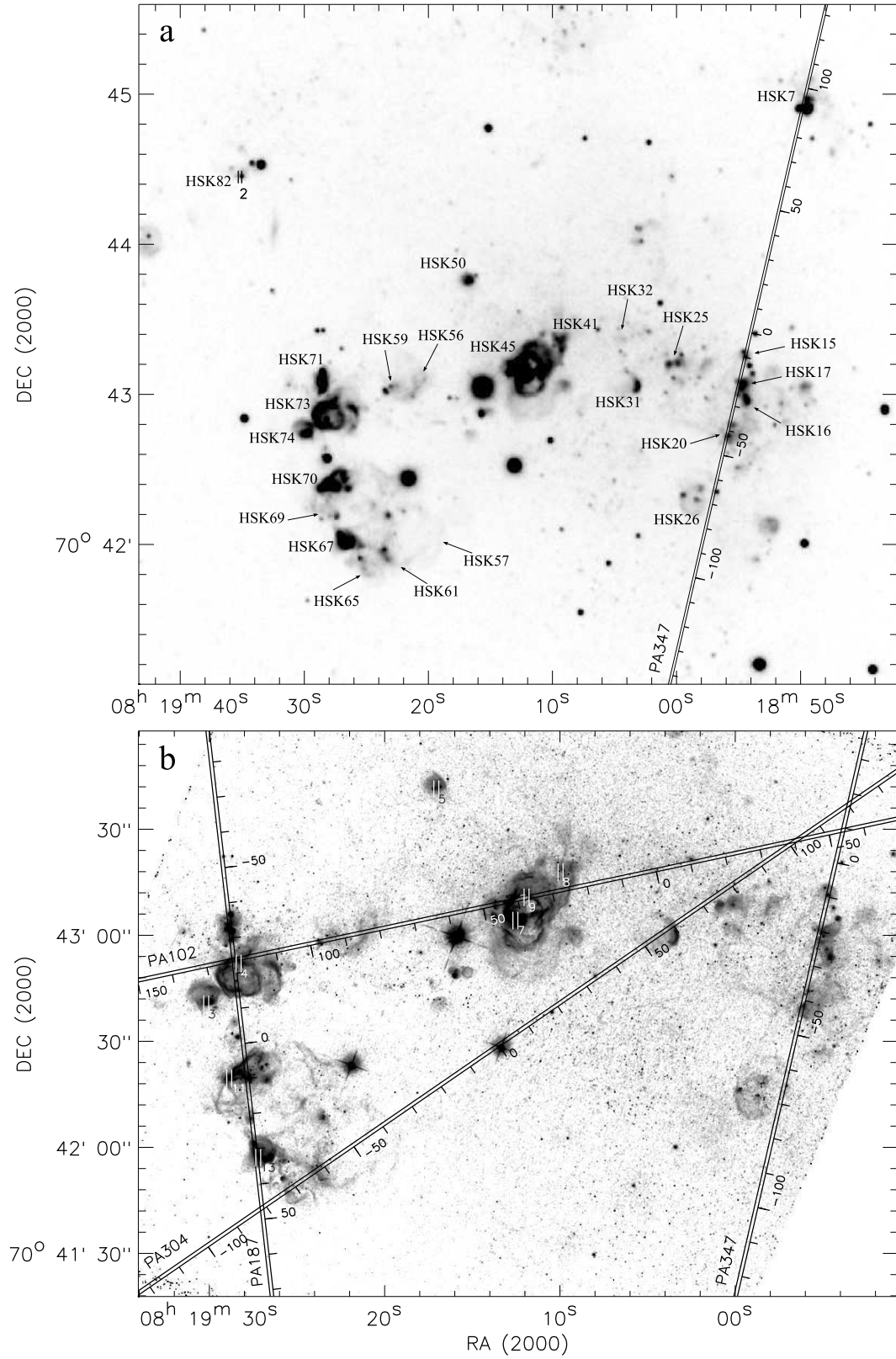


**Figure 1.** The H $\alpha$ +continuum images of the Ho II galaxy (panel ‘a’ shows the image taken with the 2.1-m KPNO telescope and panel ‘b’, archival *HST* image (F658N/ACS WFC)). Panel ‘a’ gives the designations of all H II regions discussed in this paper (denoted by the HSK numbers from the catalogue of Hodge et al. 1994), shows the position of the spectrograph slit PA347 used in our observations and the position of slit #2 in observations of Croxall et al. (2009). Panel ‘b’ shows the positions of the spectrograph slits in our observations; the short white line segments indicate the locations of the Croxall et al. (2009) spectrograms marked by their numbers in accordance with the above paper.

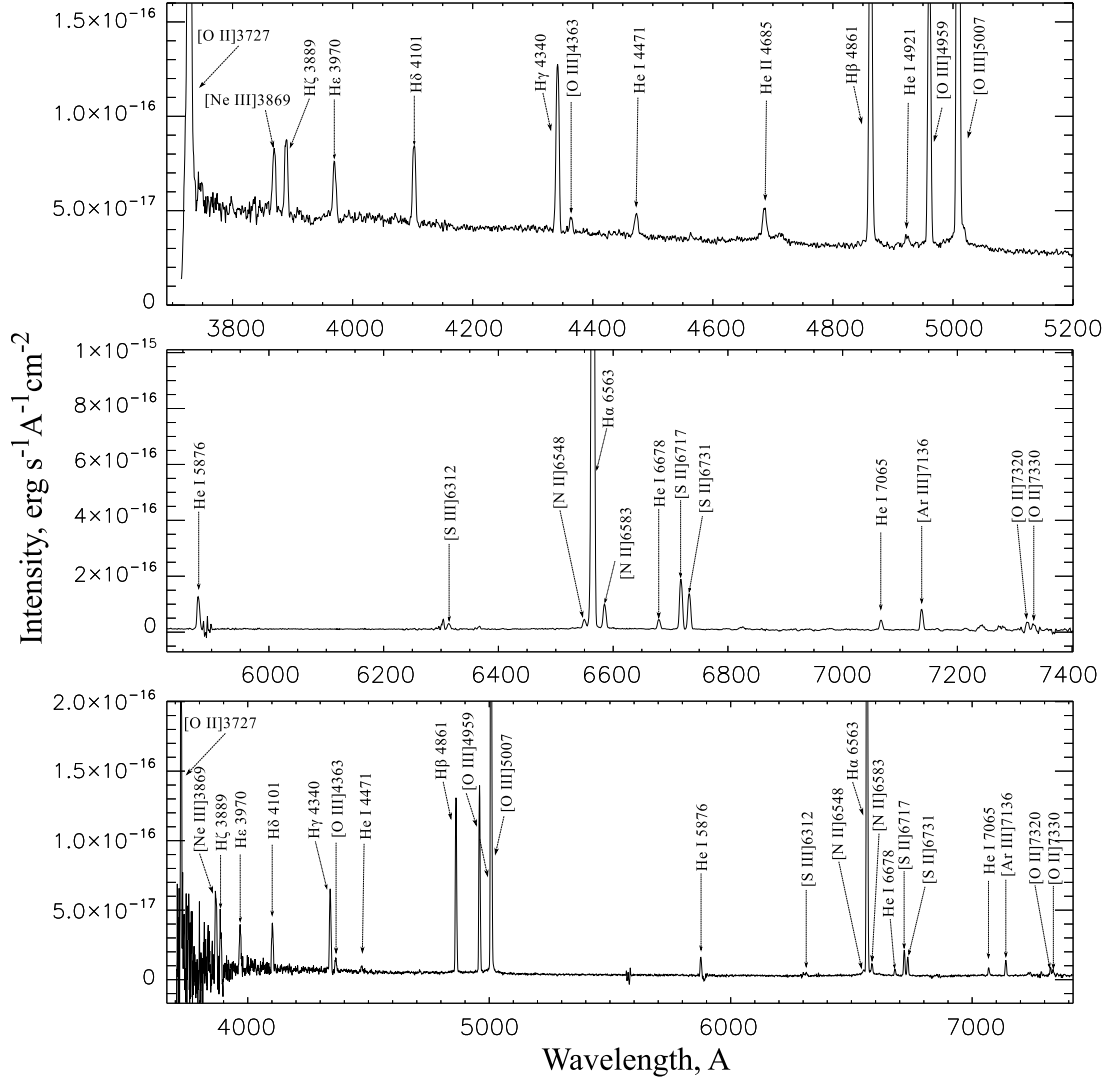


**Figure 2.** Examples of spectra taken with different SCORPIO/SCORPIO-2 grisms. The top panel shows the region between  $-21.4$  and  $-17.3$  arcsec along the PA187 slit (the central part of the HSK73 nebula, which exhibits bright emission in the He II  $\lambda 4686$  line) observed with the VPHG1200B grism; the middle panel shows the region between  $40.7$  and  $45.0$  arcsec along the PA102 slit (the HSK45 nebula) observed with the VPHG1200R grism, and the bottom panel shows the region between  $94.6$  and  $98.2$  along the PA347 slit (the HSK7 nebula) observed with the VPHG940@600 grism.

Fig. 2 shows examples of spectrograms taken with different grisms. The top panel shows the integrated spectrum of the part of the HSK73 H II region crossed by the PA187 slit (positions ranging from  $-21.4$  to  $-17.3$  arcsec along the slit) taken with the VPHG1200B grism. It is the region where we found the brightest He II  $\lambda 4686$  emission line (see section 4). The middle panel shows the integrated spectrum of the eastern boundary of HSK45, which is the brightest nebula in the galaxy, taken with the VPHG1200R grism (the PA102 spectrogram, positions ranging from  $40.7$  to  $45.0$  arcsec). The bottom panel shows the integrated spectrum of the HSK7 region taken with the VPHG940@600 grism (the PA347 spectrogram, positions ranging from  $94.6$  to  $98.2$  arcsec). The spectrum of this region is of the highest quality among all the spectra taken with this grism within the framework of this study (in the vicinity of the [O II]  $\lambda 3727$  and [O III]  $\lambda 4363$  lines its signal-to-noise ratio is as high as 6–7).

Due to the wide spectral range of the VPHG940@600

grism there is possible second order contamination on the spectra obtained with this grism at wavelengths redder than  $7000$  Å. But consideration of the continuum at this range (see, for example, bottom panel of the Fig. 2) shows that possible systematic errors of emission line intensity measurements is no more than 12% and lies in the uncertainties reported further.

To ensure the homogeneity of the inferred gas metallicities in the galaxy, we also use the relative line intensities reported by Lee et al. (2003) and Croxall et al. (2009). Lee et al. (2003) do not specify the locations of the spectra and only give the names of the H II regions studied. Figure 1 shows the locations of the spectra taken by Croxall et al. (2009) (we adopt the coordinates from the author-corrected astro-ph electronic version of the paper). The spectrograms are numbered in accordance with Croxall et al. (2009).

Table 2 lists our estimated relative emission-line intensities in the individual H II regions. We determined these

intensities by integrating the spectrum along the part of the nebula crossed by the slit. The intensities are measured relative to the  $H\beta$  line intensity assuming that  $I(H\beta) = 100$ .

We obtained two spectrograms for the PA187 slit. One of them, like in the case of PA304 and PA347, covers the entire spectral range from the blue to the red part, whereas the other one contains only the blue part of the spectrum (see Table 1). The two spectrograms were taken on different nights with varying seeing using different instruments equipped with different CCDs. Hence a question naturally arises whether the two spectra are on the same intensity scale. We compared the line intensities in the blue part of the spectrum for each H II region as estimated from both spectrograms and found their intensity scales to be proportional to each other. Hence albeit the line intensities measured by different spectrograms differ from each other, the ratios of the emission line intensities to the  $H\beta$  flux are the same for both spectra within the observational errors. That is why in the case of PA187 Table 2 lists relative line intensities measured either by the ‘wide-range’ spectrogram taken with the VPHG940@600 grism or by the spectrogram taken with the VPHG1200B grism depending on the line wavelength. The intensities measured by spectra taken with the ‘wide-range’ VPHG940@600 grism are used for lines located on the red side of [O III]  $\lambda 5007$ , and those measured by the spectra taken with the VPHG1200B grism are used for lines in the blue part of the spectrum, where the sensitivity of the VPHG940@600 grism decreases.

The situation with PA102 is more complicated, because in this case two spectrograms have been taken for the blue and red parts of the spectrum and their spectral ranges do not overlap, preventing a similar comparison. Therefore to correctly estimate the ratios of line intensities on the red side of [O III]  $\lambda 5007$  to  $H\beta$ , we calculated the ratios of the corresponding line intensities to  $H\alpha$  and used the ‘theoretical’  $I(H\alpha)/I(H\beta) = 2.809$  ratio for the average electron temperature  $T_e = 13000$  K (Osterbrock & Ferland 2006).

The line intensity ratios listed in Table 2 are reddening corrected. We determined the  $E(B - V)$  colour index from the Balmer decrement using the theoretical intensity ratios  $I(H\alpha)/I(H\beta) = 2.809$  and  $I(H\gamma)/I(H\beta) = 0.4745$  for the electron temperature  $T_e = 13000$  K (Osterbrock & Ferland 2006) and the extinction curve of Cardelli et al. (1989) as parametrised by Fitzpatrick (1999). For the PA102 slit we used only the  $I(H\gamma)/I(H\beta)$  ratio. The resulting  $E(B - V)$  extinction values are listed in Table 3.

Our inferred colour excesses  $E(B - V)$  are greater than the  $E(B - V) = 0.06 \pm 0.04$  estimate reported by Croxall et al. (2009). We obtained a similar extinction value  $E(B - V) = 0.03$  towards Holmberg II from the extinction map based on the data of the infrared sky survey (Schlegel et al. 1998).

The mean colour index averaged over all our spectrograms is  $E(B - V) = 0.17 \pm 0.08$ . It differs from the estimate of Croxall et al. (2009) and this can be due to the use of different extinction laws. Our inferred  $E(B - V)$  value possibly corresponds to the stronger local extinction, because all the bright H II regions studied are located in the direction of the maximum H I column density in the ‘walls’ of a giant cavity, and, most likely, are partially embedded in this dense supershell.

### 3.1 Estimation of the electron density and temperature.

Our electron density  $n_e$  and electron temperature  $T_e$  estimates for a number of H II regions in Holmberg II have large uncertainties.

Table 3 lists the electron densities  $n_e$  for each H II region derived from the [S II]  $\lambda 6717/\lambda 6731$  line intensity ratio. This line intensity ratio proved to be very close to the limiting value for low densities and therefore we could determine  $n_e$  in a number of H II regions only very approximately.

We determined the electron temperatures in H II regions in terms of the so-called two-zone model assuming that  $T_e$  in the low and high ionization zones is the same for all ions whose radiation emerges from these regions. Correspondingly, we assume that the temperature in the high-ionization region (for the  $O^{2+}$  and  $Ne^{2+}$  ions) is equal to  $T_e(O III)$ , and the temperature in the low-ionization region (for the  $O^+$ ,  $N^+$ , and  $S^+$  ions) is equal to  $T_e(O II)$ . We also adopt the common extension of the model proposed by Garnett (1992), which assumes that the temperature inside the region of the  $S^{2+}$  and  $Ar^{2+}$  emission is equal to the temperature  $T_e(S III)$ .

We calculate the  $T_e(O III)$  temperature from the [O III] ( $\lambda 4959 + \lambda 5007$ )/[O III]  $\lambda 4363$  line intensity ratio (Osterbrock & Ferland 2006). However, because of the low intensity of the [O III]  $\lambda 4363$  line we could determine  $T_e(O III)$  accurately enough only for 10 H II regions (including two different parts of the HSK73 nebula) by the relation of Pilyugin et al. (2010):

$$t = \frac{1.467}{\log Q_3 - 0.867 - 0.193 \log t + 0.033t},$$

where  $Q_3 = I_{[O III](\lambda 4959 + \lambda 5007)}/I_{[O III]\lambda 4363}$  and  $t = 10^{-4}T_e(O III)$ .

We estimate the  $T_e(O II)$  temperature in low-ionization regions by the [O II] ( $\lambda 3727 + \lambda 3729$ )/[O II] ( $\lambda 7320 + \lambda 7330$ ) line intensity ratio using the following relation of Pilyugin et al. (2009):

$$t_2 = \frac{0.96}{\log Q_2 - 0.86 - 0.38 \log t_2 + 0.053t_2 + \log(1 + 14.9x)},$$

where  $x = 10^{-4}n_e t_2^{-1/2}$ ,  $t_2 = 10^{-4}T_e(O II)$ , and  $Q_2 = I_{[O II](\lambda 3727 + \lambda 3729)}/I_{[O II](\lambda 7320 + \lambda 7330)}$ .

While determining  $T_e(O II)$  we had to address a number of problems. First, in observations of nearby objects, such as Holmberg II, the [O II]  $\lambda 7320 + \lambda 7330$  emission feature falls within the domain of strong atmospheric hydroxyl absorption lines, which reduce the accuracy of the intensity measurements for these lines and hence that of the inferred  $T_e(O II)$ . Our failure to properly subtract the contribution of the air glow lines in the spectra of some H II regions makes the corresponding [O II]  $\lambda 7320 + \lambda 7330$  intensity estimates less reliable.

Second, the sensitivity of the CCD used in half of the observations decreases sharply in the blue part of the spectrum. This prevented us from measuring the [O II]  $\lambda 3727 + \lambda 3729$  lines accurately enough in the PA304 and PA347 spectra, making it impossible to calculate  $T_e(O II)$ . In the case of the PA102 and PA187 spectra we derived

the temperature in the low-ionization regions only in four H II regions, where the signal-to-noise ratio in the [O II]  $\lambda 7320 + \lambda 7330$  lines was greater than 4.

We could thus ‘directly’ determine the electron temperatures both in the low- and high-ionization regions only in HSK45, HSK67, HSK71, and HSK73. However, even in these nebulae the inferred  $T_e(\text{O II})$  estimates are not accurate and most likely represent the upper temperature limits for the corresponding regions. We therefore used empirical methods to infer the temperatures in low-ionization regions in the cases where we could determine  $T_e(\text{O III})$ .

Many methods are known for the empirical determination of electron temperature in low-ionization regions from the known  $T_e(\text{O III})$  temperature. Hägele et al. (2008) compared some of the methods used to estimate the temperature in the  $\text{O}^+$  emission region. Pérez-Montero & Díaz (2003) pointed out that this temperature is strongly dependent not only on  $T_e(\text{O III})$ , but also on the electron density  $n_e$ . This imposes strong constraints on the applicability of the empirical  $T_e(\text{O II})$  on  $T_e(\text{O III})$  dependences. In particular, we did not use the dependence of  $T_e(\text{O II})$  on  $T_e(\text{O III})$  found by Pérez-Montero & Díaz (2003) for three electron density values,  $n_e = 10, 100$ , and  $500 \text{ cm}^{-3}$ , because of the above-mentioned low accuracy of the estimated  $n_e$ .

Stasińska (1980, 1990) proposed a method, which gained widespread popularity. Izotov et al. (2006) proposed to determine the temperature in regions with ionization higher and lower than in the  $\text{O}^{2+}$  emission region using a technique depending on the gas metallicity. Furthermore, Pilyugin et al. (2009) proposed an empirical formula for estimating  $T_e(\text{O II})$  and  $T_e(\text{N II})$  from  $T_e(\text{O III})$ . These authors point out that the  $T_e(\text{N II})$  value should be preferred for the low-ionization regions because of its lower dispersion. López-Sánchez et al. (2012) proposed a calibration based on the model spectra of H II regions.

We used all the above mentioned methods to determine the temperatures in the low-ionization regions. We found the calibration of López-Sánchez et al. (2012) to be the most consistent with the estimate determined from the spectra of four H II regions, which represents an upper limit for the  $T_e(\text{O II})$  temperature in these nebulae. Hereafter throughout this paper we adopt the estimates obtained using the above technique obtained by the relation:

$$T_e(\text{O II}) = T_e(\text{O III}) + 450 - 70 \exp[(T_e(\text{O III})/5000)^{1.22}].$$

The temperatures  $T_e(\text{O II})$  estimated by other methods are much higher than our inferred upper constraints for four H II regions.

The dependence of the temperature in the  $\text{S}^{2+}$  emission region on  $T_e(\text{O III})$  has a much lower scatter than the corresponding dependence for low-ionization regions (see, e.g., Hägele et al. 2008). We estimated  $T_e(\text{S III})$  using the equation proposed by Izotov et al. (2006) for different H II region metallicities:

$$\begin{aligned} t_3 &= -1.085 + t \times (2.320 - 0.420t), \text{ for } 12 + \log(\text{O}/\text{H}) \simeq 7.2, \\ &= -1.276 + t \times (2.645 - 0.546t), \text{ for } 12 + \log(\text{O}/\text{H}) \simeq 7.6, \\ &= 2.967 + t \times (-2.261 + 1.605t), \text{ for } 12 + \log(\text{O}/\text{H}) \simeq 8.2, \end{aligned}$$

where  $t_3 = 10^{-4}T_e(\text{S III})$ ,  $t = 10^{-4}T_e(\text{O III})$ .

Table 3 lists the adopted electron temperatures in the regions of different ionization.

### 3.2 Estimation of the gas metallicity

Currently, many methods are used to estimate the abundances of chemical elements and primarily that of oxygen, which determines the metallicity of the interstellar medium. The most popular is the so-called ‘direct’, or  $T_e$  method, which allows elemental abundances to be estimated from the forbidden-line intensity ratios provided that the electron temperature  $T_e$  is known in the region where the corresponding emission line forms. However, we cannot always use this method since we have direct spectra-based electron temperature estimates in the zones of different ionization solely for four H II regions. Only in 10 regions the temperatures in low-ionization zones were estimated using empirical methods. We therefore used the  $T_e$  method to estimate the relative abundances of the  $\text{O}^+$ ,  $\text{O}^{2+}$ ,  $\text{N}^+$ ,  $\text{S}^+$ ,  $\text{S}^{2+}$ ,  $\text{Ar}^{2+}$ , and  $\text{Ne}^{2+}$  ions in these regions wherever the signal-to-noise ratio for the corresponding ion lines was greater than 3.

We estimated the relative ion abundances using the relations from studies based on modern atomic data: we used the equations from Pilyugin et al. (2010) to compute the abundances of  $\text{O}^+$  and  $\text{O}^{2+}$  ions, and those from Izotov et al. (2006), to compute the  $\text{N}^+$ ,  $\text{S}^+$ ,  $\text{S}^{2+}$ ,  $\text{Ar}^{2+}$ , and  $\text{Ne}^{2+}$  ionic abundances. For the unobserved ionization stages we calculated the ionization correction factors (*ICF*) by the relations adopted from Izotov et al. (2006), which allowed us to determine the abundances of oxygen, sulphur, argon, and neon.

Among the popular metallicity determination methods there are those based on the intensity ratios of bright emission lines. These include the so-called ‘empirical’ methods calibrated by H II regions with bona fide oxygen abundance estimates and methods based on theoretical photoionization models. In this paper we use six such methods:

(i) The PT05 method (Pilyugin & Thuan 2005), where the oxygen abundance is fitted by a function of  $R_2 = I_{[\text{O II}]\lambda 3727 + \lambda 3729}/I_{\text{H}\beta}$ ,  $R_3 = I_{[\text{O III}]\lambda 4959 + \lambda 5007}/I_{\text{H}\beta}$ ,  $R_{23} = R_2 + R_3$ , and the excitation parameter  $P = R_3/(R_3 + R_2)$ . It is one of the most widely used empirical methods with the applicability domain confined to the  $0.55 < P < 1$  interval;

(ii) The ONS method (Pilyugin et al. 2010), which allows the oxygen and nitrogen abundances to be determined as a function of parameters  $R_2$ ,  $R_3$ ,  $N_2 = I_{[\text{N II}]\lambda 6548 + \lambda 6583}/I_{\text{H}\beta}$ ,  $S_2 = I_{[\text{S II}]\lambda 6717 + \lambda 6731}/I_{\text{H}\beta}$ , and  $P$ ;

(iii) The ON method (Pilyugin et al. 2010), which is similar to the ONS method, but does not require the knowledge of  $S_2$ ;

(iv) The NS method (Pilyugin & Mattsson 2011), which does not require [O II]  $\lambda 3727 + \lambda 3729$  intensity measurements and allows the oxygen and nitrogen abundances to be determined as functions of parameters  $R_3$ ,  $N_2$ , and  $S_2$ ;

(v) The PP04 method (Pettini & Pagel 2004), which allows the relative oxygen abundance to be determined from the parameter  $O_3N_2 = \log[(I_{[\text{O III}]\lambda 5007}/I_{\text{H}\beta})/(I_{[\text{N II}]\lambda 6583}/I_{\text{H}\alpha})]$ . This method is practically extinction independent; it works in the  $-1 < O_3N_2 < 1.9$  interval;

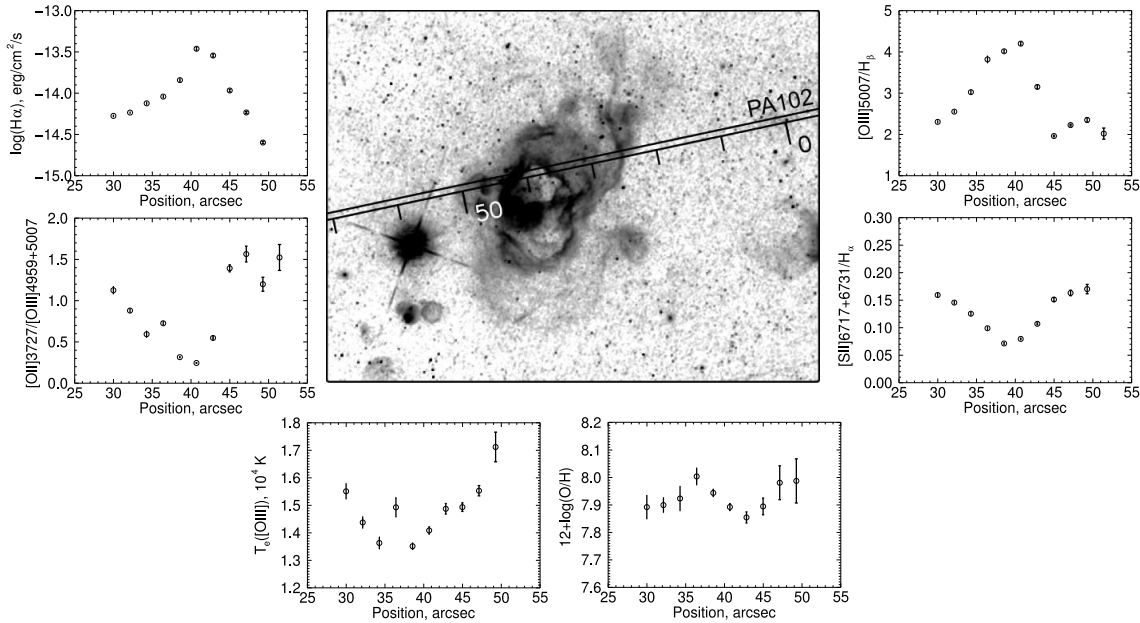


**Figure 3.** The H II region HSK45. The central part of the figure shows the *HST* H $\alpha$  image together with the position of the PA102 slit. The left, right, and bottom panels show the distribution of relative emission-line intensities, electron temperature, and oxygen abundance, respectively, along the portion of the slit crossing the HSK45 region.

(vi) The KK04 method (Kewley & Dopita 2002 with the new parametrisation by Kobulnicky & Kewley 2004) based on theoretical photoionization models, which can be used to determine the oxygen abundance as a function of parameter  $R_{23}$  and ionization parameter  $q$ , which, in turn, can be obtained from the  $O_{32} = I_{[O III] \lambda 4959 + \lambda 5007} / I_{[O II] \lambda 3727 + \lambda 3729}$  line intensity ratio.

All the above methods can be used to determine the oxygen abundances,  $12 + \log(O/H)$  in the H II regions. According to the authors of original publications, these methods are accurate to about 0.1 dex (the PP04 method is less accurate, its error is of about 0.2–0.25 dex; the ON, NS, and ONS methods have smaller errors – of about 0.075 dex). The ON, NS, and ONS methods can also be used to determine the nitrogen abundance and hence the  $\log(N/O)$  abundance ratio, which is important for chemical evolution models of galaxies.

The chemical abundances of the Holmberg II H II regions were earlier estimated by Masegosa et al. (1991); Lee et al. (2003), and Croxall et al. (2009). Moustakas et al. (2010) summarised these results and reported the galaxy-averaged abundances and average abundances at different galactocentric distances. We use all these data to compare with our results.

Croxall et al. (2009) and Lee et al. (2003) report relative line intensities, which we used to determine the elemental abundances by applying all the methods employed in this paper.

Table 3 lists the resulting estimates of abundances of chemical elements and individual ions for the H II regions based on our observations and line intensities reported by Croxall et al. (2009) and Lee et al. (2003). Table 3 gives only the formal measurement errors, which do not include the uncertainties of the each method itself.

Abundances obtained for similar slit positions based on our observations and those reported in previous studies mostly agree well with each other within the quoted observational errors. The oxygen abundances reported by Croxall et al. (2009) and Lee et al. (2003) slightly differ from those calculated in this study using the fluxes reported by the above authors. This discrepancy is due to the use of different atomic data. For some H II regions, the abundances determined in this paper do not match those obtained by Croxall et al. (2009) and Lee et al. (2003) because we observed different parts of the nebulae, which show significant abundance variations (see Section 4.1).

## 4 DISCUSSION

### 4.1 Emission spectra of individual H II regions

We analysed the variations of the emission-line intensity and physical conditions inside the H II regions in the brightest nebulae HSK45, HSK73, HSK70, and HSK67. Note that the detailed distribution of metallicity along an individual nebula could be determined only using the ‘direct’ method. Empirical methods can be applied only to the entire nebula as a whole – when they are used to determine the local chemical composition, the results are seriously affected by the emission stratification inside the region.

**HSK45.** This is the largest H II complex seen in the H $\alpha$  images of the galaxy. Its angular size is of about 25–30 arcsec, corresponding to the linear size of 410–490 pc. According to the estimates of Stewart et al. (2000), it is a young region with an age of 2.5–3.5 Myr. Its composite multishell structure conspicuously shows up in the images.

Fig. 3 shows the image of the HSK45 H II region and the distribution of diagnostic line ratios along the part of the PA102 slit crossing the nebula. The  $[O III] \lambda 4959 + \lambda 5007/H\beta$

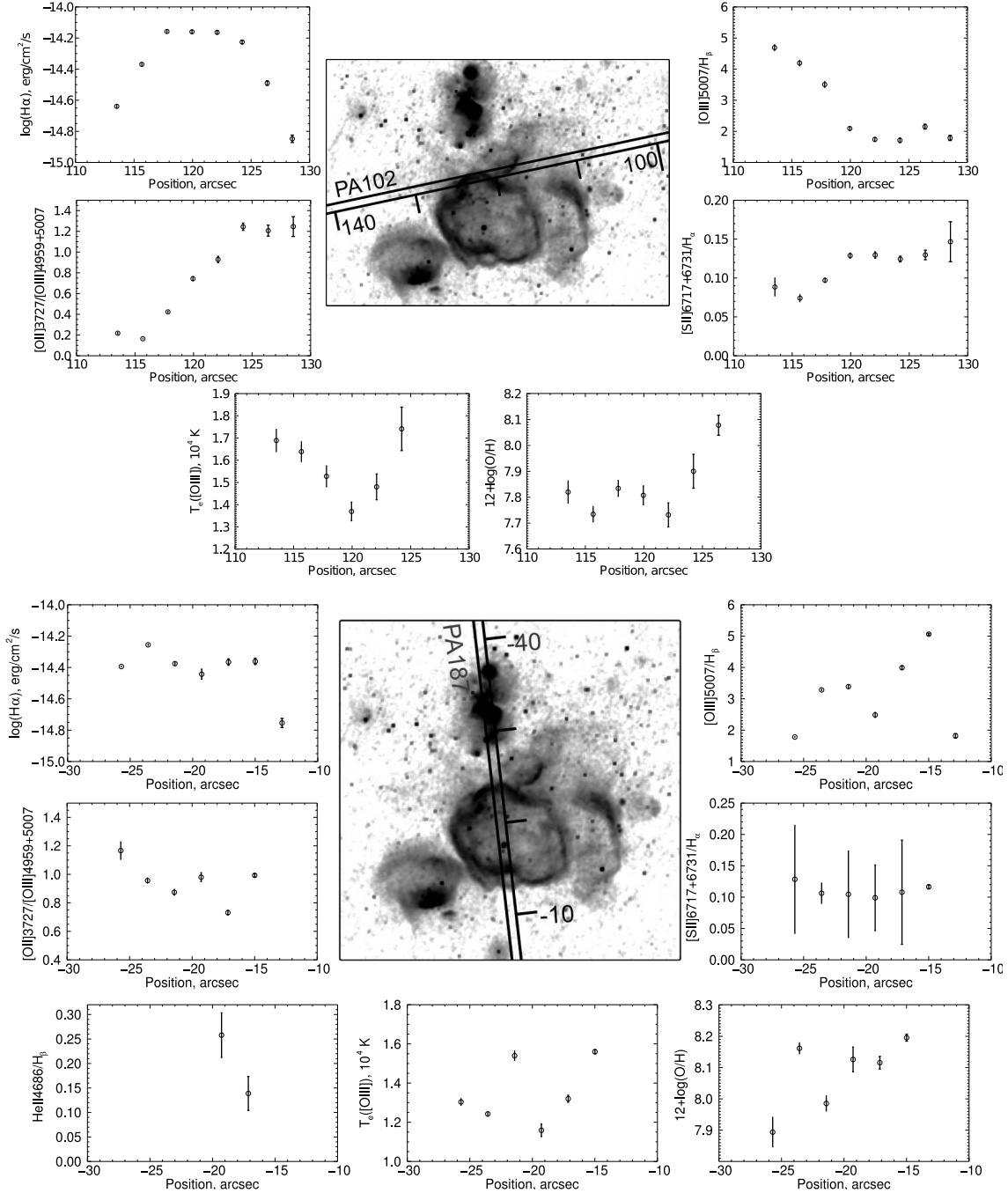


**Figure 4.** The H II region HSK73. The top and bottom panels show the results obtained along the PA102 and PA187 slits, respectively. The central part of each figure shows the *HST* H $\alpha$  image and the corresponding slit position. Each figure shows the distribution of relative emission-line intensities, electron temperature, and oxygen abundance along the part of the slit crossing this region.

intensity ratio in the crossed parts of the shells is equal to about 2 and reaches 4.5 in the faint central area. The gas ionization degree at the centre is higher than at the edges of the complex. The decrease of the [O III]  $\lambda 4959 + \lambda 5007/H\beta$  ratio at the periphery can be explained by the fact that the oxygen emission there is dominated by  $O^+$ , and the decrease of the [S II]  $\lambda 6717 + \lambda 6731/H\alpha$  toward the centre of the region could be caused by the high ionization stage of sulphur represented by  $S^{2+}$  (possibly, in the vicinity of an ionizing cluster).

The HSK45 region exhibits a non-uniform distribution of  $T_e$  along the slit. The relative oxygen abundance also varies along the region, however, these variations are not so strong, and metallicity is more or less constant and consistent with the region-averaged value listed in Table 3.

**HSK 73.** This region, like HSK45, is one of the brightest and most extended among those seen in the H $\alpha$  image of the galaxy (see Fig. 1). The complex has an angular size of about 15–20 arcsec (linear size 250–330 pc). It is also a young region with an age of about  $t = 2.5 - 3.5$  Myr (Stewart et al.



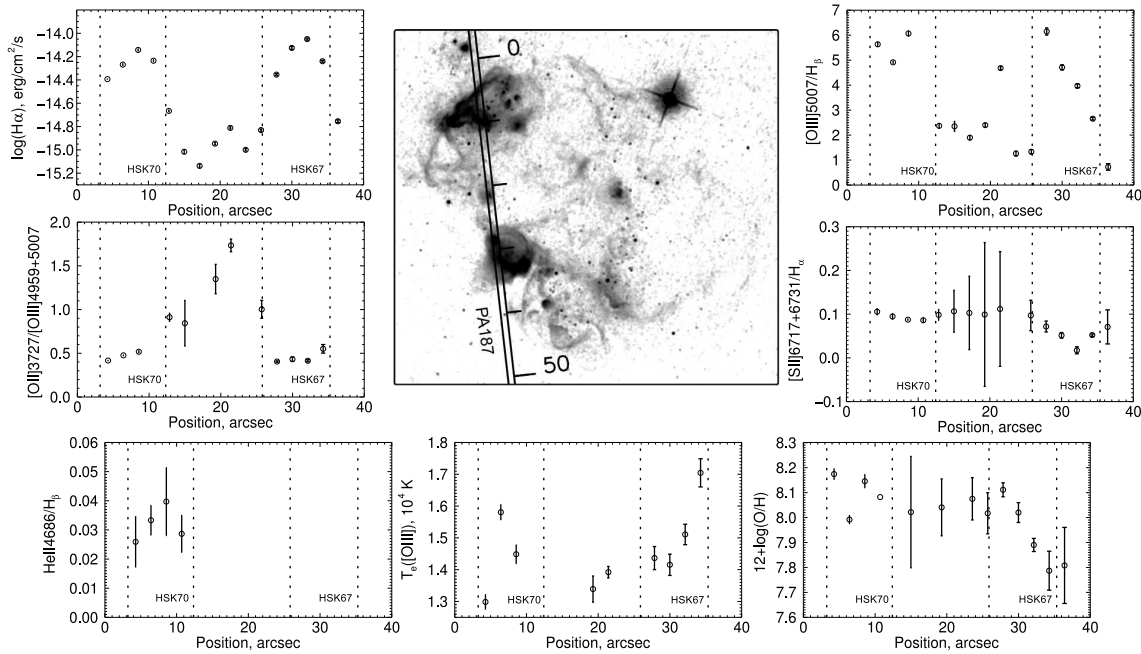


**Figure 5.** The H II regions HSK70 and HSK67. The central part of the figure shows the  $H\alpha$  image (taken from the *HST* archive). Also shown is the position of the PA187 slit. The other panels show the distribution of relative emission-line intensities, electron temperature, and oxygen abundance along the slit.

2000), characterised by a composite shell structure. The centre of the region hosts the most massive stellar cluster of those studied by Cook et al. (2012) in the HoII galaxy.

Fig. 4 shows the image of the HSK73 region and the distribution of relative emission-line intensities, the electron temperature and oxygen abundance along the parts of the PA102 and PA187 slits crossing the complex from west to east and from north to south, respectively.

The  $[\text{O III}] \lambda 4959 + \lambda 5007/H\beta$  intensity ratio is constant in the north-eastern part of the region and increases significantly in its north-western part; this ratio can also be seen to increase from north to south. The  $[\text{O II}] \lambda 3727/[\text{O III}] \lambda 4959 + \lambda 5007$  ratio, which characterises the degree of gas ionization, decreases with increasing  $[\text{O III}] \lambda 4959 + \lambda 5007/H\beta$ . This behaviour indicates that gas ionization is higher in the north-western and southern parts of the region and that the cause is photoionization.

We found a rather bright He II  $\lambda 4686$  line emission in the central part of the region (positions ranging from  $-17$  to  $-20$  arcsec on the PA187 slit). Note that the helium line emission region is compact and no such emission is present in the spectrum of the outer shell. The He II line emission may supposedly be due to the fact that here the slit crosses a compact nebula ionised by a Wolf-Rayet star or by another source of intense ultraviolet radiation.

The distribution of oxygen abundance along the portions of the PA102 and PA187 slits crossing HSK73 demonstrates a constant gas metallicity in the north-western outskirts of the region and a possible north-to-south metallicity gradient. Oxygen abundance also increases sharply near the north-eastern part of the shell.

**HSK 70 and HSK 67.** These two H II regions are more compact than HSK45 and HSK73: the size of HSK70 is of about 10–15 arcsec (160–250 pc) and that of HSK67, about

8 arcsec (130 pc). Stewart et al. (2000) estimated the ages of these regions to be 3.5–4.5 and 2.5–3.5 Myr, respectively.

Fig. 5 shows the *HST*  $H\alpha$  images of HSK70 and HSK67, the position of the PA187 spectrograph slit, and the distribution of relative line intensities, electron temperature, and oxygen abundance along the slit.

The image of the extended surroundings of HSK70 and HSK67 reveals a faint shell-like structure with a size of 40–50 arcsec (650–820 pc), which includes the two bright nebulae.

The only known ultraluminous X-ray source (ULX) in the galaxy, Holmberg II X-1, is located at the eastern boundary of the HSK70 region. This source completely determines the kinematics and emission spectrum of the region (for a detailed study of the nebula surrounding the source see Lehmann et al. 2005). The spectrograph slit in our observations crosses the region 5 arcsec West of the source, but even at this distance (80 pc) a strong He II  $\lambda 4686$  line emission of the nebula surrounding the ULX is observed (see Fig. 5).

The  $[\text{O III}] \lambda 4959 + \lambda 5007/H\beta$  intensity ratio is high inside the two bright H II regions and decreases in the space between them. The  $[\text{O II}] \lambda 3727/[\text{O III}] \lambda 4959 + \lambda 5007$  ratio, on the contrary, is low inside the regions and higher in the space between. This fact indicates that gas ionization inside HSK70 and HSK67 is higher than in the outskirts of the two bright nebulae.

Gas metallicity in the HSK70 and in its outskirts is more or less the same and coincides with the region-averaged value. The HSK67 nebula exhibits a sharp decrease of oxygen abundance in the north-south direction.

The  $[\text{S II}] \lambda 6717 + \lambda 6731/H\alpha$  line intensity ratio does not exceed 0.2 along all the regions described above, thereby supporting the photoionization mechanism of gas excitation.

**Table 2.** Oxygen abundances in the IC 10 and VII Zw 403 galaxies estimated using different methods

Galaxy	H II region & slit PA	$T_e$	12 + log(O/H) estimated using different methods					
			PT05	ONS	ON	NS	PP04	KK04
IC 10	HL111a PA0	$8.28 \pm 0.04$	$8.34 \pm 0.24$	$8.14 \pm 0.06$	$8.05 \pm 0.05$	$8.16 \pm 0.02$	$8.36 \pm 0.01$	$8.27 \pm 0.28$
IC 10	HL111b PA0	$8.29 \pm 0.04$	$8.27 \pm 0.22$	$8.18 \pm 0.06$	$8.11 \pm 0.05$	$8.22 \pm 0.03$	$8.41 \pm 0.01$	$8.23 \pm 0.29$
IC 10	HL111c PA0	$8.24 \pm 0.02$	$8.24 \pm 0.15$	$8.03 \pm 0.03$	$7.92 \pm 0.03$	$8.07 \pm 0.01$	$8.18 \pm 0.04$	$8.38 \pm 0.11$
IC 10	HL111e PA0	$8.24 \pm 0.07$	$8.29 \pm 0.38$	$8.12 \pm 0.12$	$8.05 \pm 0.09$	$8.15 \pm 0.04$	$8.29 \pm 0.01$	$8.28 \pm 0.45$
IC 10	HL111d PA268	$8.05 \pm 0.05$	$8.28 \pm 0.11$	$8.12 \pm 0.05$	$8.07 \pm 0.04$	$8.16 \pm 0.03$	$8.26 \pm 0.05$	$8.33 \pm 0.08$
IC 10	HL111c PA268	$8.15 \pm 0.03$	$7.94 \pm 0.10$	$7.86 \pm 0.03$	$7.71 \pm 0.03$	$7.70 \pm 0.03$	$8.18 \pm 0.01$	$8.32 \pm 0.02$
IC 10	HL111a PA331	$8.20 \pm 0.04$	$8.05 \pm 0.34$	$8.14 \pm 0.09$	$8.17 \pm 0.07$	$8.19 \pm 0.03$	$8.13 \pm 0.01$	$8.35 \pm 0.23$
IC 10	HL50 PA331	$8.19 \pm 0.20$	$8.30 \pm 0.16$	$8.07 \pm 0.34$	$8.04 \pm 0.31$	$8.01 \pm 0.13$	$8.42 \pm 0.01$	—
IC 10	HL45 PA45	$8.15 \pm 0.05$	$7.92 \pm 0.17$	$7.79 \pm 0.10$	$7.84 \pm 0.08$	$7.84 \pm 0.04$	$8.31 \pm 0.01$	$8.16 \pm 0.20$
IC 10	HL50 PA45	$8.25 \pm 0.02$	$8.10 \pm 0.16$	$8.24 \pm 0.03$	$8.27 \pm 0.02$	$8.29 \pm 0.01$	$8.23 \pm 0.01$	$8.35 \pm 0.10$
VII Zw 403	#1	$7.71 \pm 0.01$	$7.43 \pm 0.03$	$7.72 \pm 0.02$	$7.80 \pm 0.02$	$7.77 \pm 0.01$	$7.96 \pm 0.03$	$7.90 \pm 0.18$
VII Zw 403	#3	$7.73 \pm 0.01$	$7.61 \pm 0.09$	$7.68 \pm 0.02$	$7.61 \pm 0.02$	$7.62 \pm 0.01$	$8.06 \pm 0.02$	$8.02 \pm 0.19$
VII Zw 403	#4	$7.75 \pm 0.02$	$7.71 \pm 0.05$	$7.71 \pm 0.03$	$7.65 \pm 0.04$	$7.67 \pm 0.03$	$8.05 \pm 0.02$	$8.09 \pm 0.14$

Note. The H II regions in IC 10 are designated in accordance with the list of Hodge & Lee (1990) and by the position angle of the spectrograph slit in our observations of this galaxy (Lozinskaya et al. 2009; Arkhipova et al. 2011). The H II regions of VII Zw 403 are identified by their numbers used in our previous studies (Arkhipova et al. 2007; Egorov & Lozinskaya 2011).

#### 4.2 Comparison of different methods of oxygen abundance determination

In recent years several authors performed detailed comparisons of different methods of elemental abundance estimation in order to determine the bona fide applicability domain of every particular method (see, e.g., Kewley & Ellison 2008, López-Sánchez et al. 2012 and references therein).

Thus the researchers have since long questioned even the correctness of the results obtained by the ‘direct’  $T_e$  method. This method may yield underestimated abundances in the case of small-scale temperature fluctuations inside the H II region (Piembert 1967) or significant temperature variations along the nebula (Stasińska 1978, 2005). A similar effect can be observed if the nebula studied is not a single Stroemgren zone, but a composite H II region containing several ionization sources<sup>2</sup>.

Pilyugin et al. (2012) showed that the  $T_e$ -method can yield overestimated N/O abundance ratios for composite nebulae, whereas the empirical ON and NS methods analysed by the above authors are free from this drawback.

López-Sánchez et al. (2012) used model spectra of H II regions to perform a detailed comparison of the currently most popular methods for estimating the chemical composition. The above authors showed that the  $T_e$  method somewhat overestimates the oxygen, neon, and argon abundances compared to the input model values. They also showed that the results of the ON, NS, and ONS methods agree excellently with those of the  $T_e$  method when applied to the spectra of real objects. However, they yield underestimated results compared to the input values when applied to model spectra. Another conclusion of López-Sánchez et al. (2012) is that the KK04 method based on photoionization models yields the results that are most consistent with the chemical composition of the stellar population. The results of this method also agree very well with those based on recombination lines. The abundances determined using the KK04

method are systematically greater than those given by the  $T_e$  method.

The Holmberg II galaxy is an excellent test ground for comparing different methods of estimating the chemical composition under the conditions of inhomogeneous and extended H II regions, where the effects like temperature variation are obviously present (see, e.g., Figs. 3, 4, 5). Indeed, most of the bright H II regions observed have angular sizes of 10 arcsec or more, implying that their linear sizes exceed 160 pc, which is evidently greater than the size of a classical Stroemgren zone around a single O-type star, and their ionization sources are young star clusters. Furthermore, the H $\alpha$  images of the galaxy reveal the shell-like structure of many of the H II regions that we observed (see Fig. 1).

Our estimates of oxygen abundance in Holmberg II H II regions based on the  $T_e$  method and six empirical methods fall in two groups (see Table 3). The first group contains the results obtained using the  $T_e$ , ON, NS, ONS, and PT05 methods (the median value  $12 + \log(\text{O}/\text{H}) = 7.73 \pm 0.13$ ), and the second group those obtained using the PP04 and KK04 methods (the median value  $12 + \log(\text{O}/\text{H}) = 8.18 \pm 0.09$ ). López-Sánchez et al. (2012) analysed model spectra and showed that the PP04 method overestimates abundances at  $12 + \log(\text{O}/\text{H}) < 8.7$  and therefore the results based on this method may be incorrect.

Our metallicity estimates obtained by applying different methods to the gas emission spectrum in Holmberg II can also be compared with the results of our earlier study of the irregular galaxy IC 10 (Lozinskaya et al. 2009; Arkhipova et al. 2011) and the BCD galaxy VII Zw 403 (Arkhipova et al. 2007; Egorov & Lozinskaya 2011). Both galaxies were observed with the 6-m telescope of the SAO RAS using the SCORPIO focal reducer operating in the long-slit spectrograph mode, and the MPFS multipupil fiber spectrograph. We used these observations to measure the relative line intensities in 26 parts of 18 H II regions in the IC 10 and in five extended H II complexes (giant H II regions) in VII Zw 403.

In the above studies we estimated the gas metallicity using the PT05, PP04, and  $T_e$  methods for the objects in IC 10

<sup>2</sup> This is the case with all the H II regions we studied in the Holmberg II galaxy.

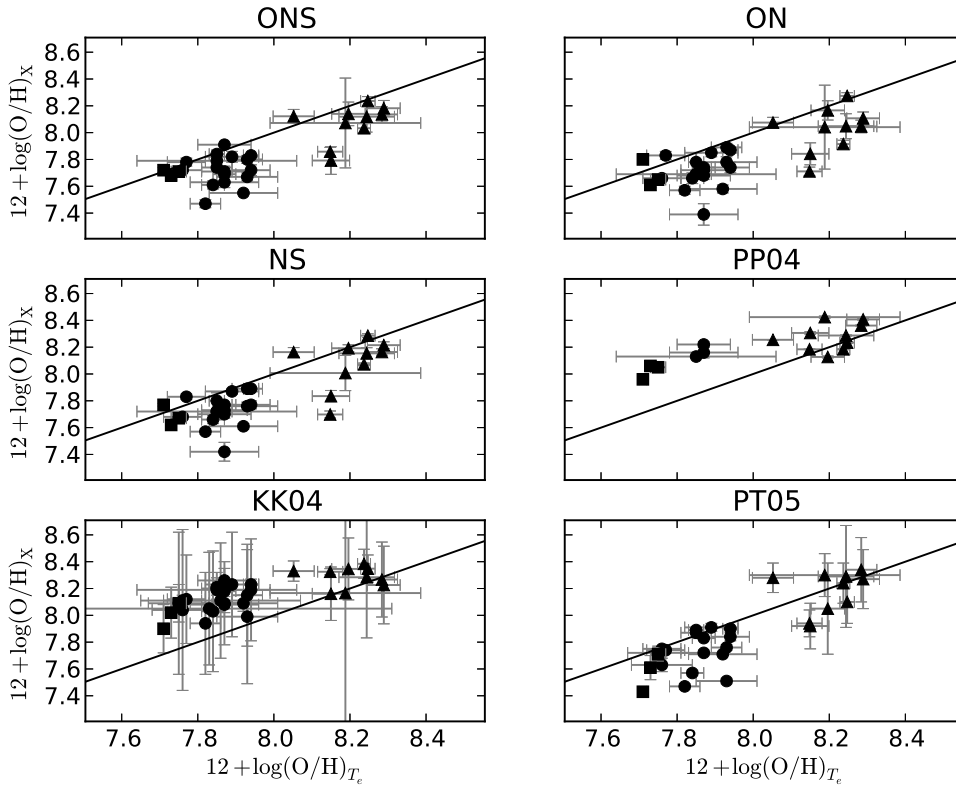


**Figure 6.** Comparison of different methods for oxygen abundance estimation with the ‘direct’  $T_e$  method. The methods are designated by the following symbols: PP04 – Pettini & Pagel (2004); KK04 – Kobulnicky & Kewley (2004); PT05 – Pilyugin & Thuan (2005); ONS and ON – Pilyugin et al. (2010); NS – Pilyugin & Mattsson (2011). The circles, triangles, and squares show the results of these methods applied to the Holmberg II, IC 10, and VII Zw 403 galaxies, respectively. The solid lines show the  $y=x$  relations for different methods.

(Lozinskaya et al. 2009; Arkhipova et al. 2011); and the ON, ONS, NS, and  $T_e$  methods for the objects in VII Zw 403 (Arkhipova et al. 2007; Egorov & Lozinskaya 2011). To correctly compare the three galaxies, we re-estimate the oxygen abundances for IC 10 and VII Zw 403 in this paper by applying all the methods that we used for Holmberg II. Note that in original papers we made certain assumptions about  $T_e$  in the H II regions when estimating the abundances in IC 10 and VII Zw 403 as described in (Lozinskaya et al. 2009) and (Egorov & Lozinskaya 2011) respectively. Our spectroscopic data allowed us to measure the intensity of the [O III]  $\lambda 4363$  line and hence the electron temperature only in one H II region HL 111 in IC 10. We adopted the  $T_e$  measurements for another two nebulae (HL 45 and HL 50) from the literature. We obtained  $T_e$  estimations from our spectra and from the literature for three H II regions in VII Zw 403. Further we use abundance measurements performed only for these regions with available  $T_e$  estimations. The oxygen abundances for these regions of IC 10 and VII Zw 403 obtained using all the methods considered are listed in Table 2.

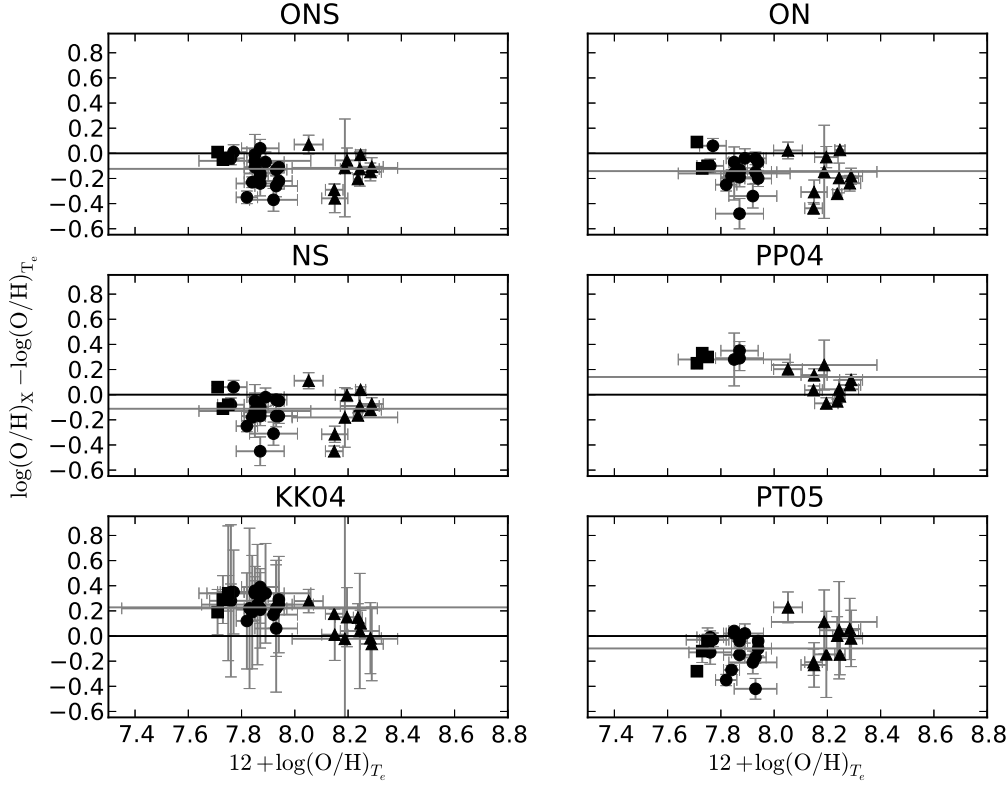
We have thus analysed a total of 34 H II regions in three galaxies using the ‘direct’  $T_e$  method and the six empirical and theoretical methods mentioned above, and present the results in Fig. 6.

Fig. 7 shows the differences between the results obtained

using these six methods as a function of the abundance determined using the direct  $T_e$  method.

It follows from Table 3 and Figs. 6 and 7 that metallicities determined using different methods indeed differ systematically, and the corresponding deviations agree well with the results of simulated ‘model’ computations by López-Sánchez et al. (2012). The estimates based on the empirical PT05, ON, NS, and ONS methods on the average agree well (although for some H II regions, the ONS method yields overestimated abundances compared to the values determined using the other two methods). Note that the PT05, ON, NS, and ONS methods somewhat underestimate the metallicities compared to the  $T_e$  method. The KK04 method, on the contrary, systematically overestimates metallicities compared to those, determined using the ‘direct’ method. The PP04 method yields similar results. We applied these methods to the model data of López-Sánchez et al. (2012) and found that the abundances determined using these techniques agree well with the metallicity estimates based on recombination lines and with the metallicity of the stellar population.

The observed variations of the estimated oxygen abundances of H II regions obtained by different methods may be due to the complex shell-like and clumpy structure of these regions. Indeed, it follows from Figs. 3, 4, and 5 that such regions exhibit appreciable, and in some cases quite



**Figure 7.** Difference between the oxygen abundance estimates obtained using the ‘direct’  $T_e$  method and the six methods mentioned above. The methods employed are designated by the following symbols: PP04 – Pettini & Pagel (2004); KK04 – Kobulnicky & Kewley (2004); PT05 – Pilyugin & Thuan (2005); ONS and ON – Pilyugin et al. (2010); NS – Pilyugin & Mattsson (2011). The circles, triangles, and squares show the results of the application of these methods to the Holmberg II, IC 10, and VII Zw 403 galaxies, respectively. The horizontal lines indicate the level of zero difference between the abundances given by the methods (black line) and the median deviation from the results of the  $T_e$  method (grey line).

important electron-temperature and metallicity variations from the centre towards the periphery. When averaged over the entire region, the results of the ‘direct’ method are more sensitive to the dense high-temperature ‘inclusions’ than to the regions with the ‘average’ density and temperature; this may explain why the direct method yields underestimated metallicities.

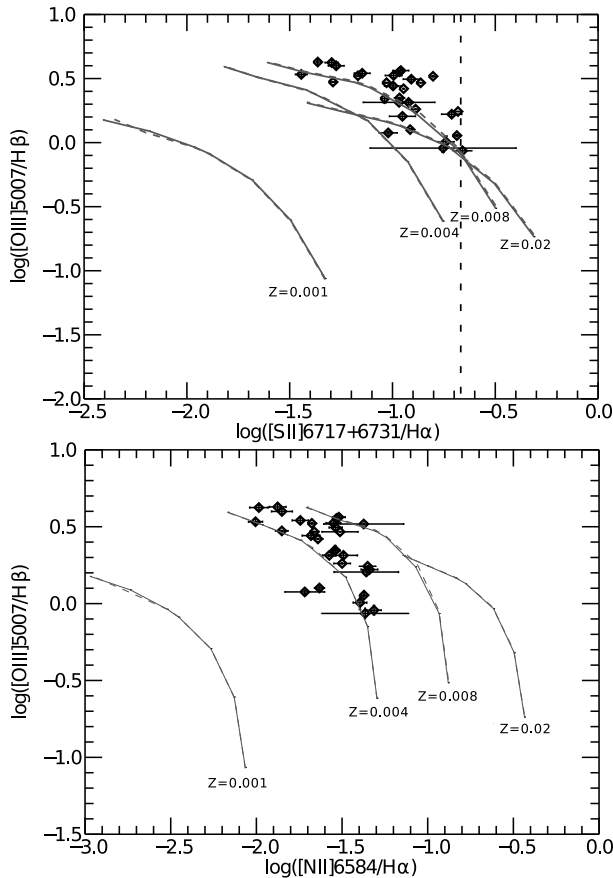
#### 4.3 Comparison of diagnostic diagrams with theoretical photoionization models.

Figure 8 shows the diagnostic diagrams of relative line intensities —  $I([\text{O III}] \lambda 5007)/I(\text{H}\beta)$  — as a function of  $I([\text{N II}] \lambda 6583)/I(\text{H}\alpha)$  or  $I([\text{S II}] \lambda 6717 + \lambda 6731)/I(\text{H}\alpha)$ . They are based on our observations of the Holmberg II galaxy and on the data of Croxall et al. (2009). These diagrams are traditionally used to compare the observations with photoionization models. The curves show the theoretical diagnostic diagrams of Kewley et al. (2010) computed for different metallicities assuming continuous star formation over 5 Myr.

It is evident from Fig. 8 that the results of observations of H II regions in the galaxy agree well with models in the metallicity interval  $Z = 0.004 - 0.008$ . Given

the current estimates of the solar metallicity,  $Z_\odot = 0.0134$  (Asplund et al. 2009), this corresponds to  $Z = (0.3-0.6)Z_\odot$ . However, the mean oxygen abundance in the galaxy estimated using the  $T_e$ , ON, NS, ONS and PT05 methods is  $12 + \log(\text{O}/\text{H}) = 7.73 \pm 0.13$ , which yields  $Z \simeq 0.1Z_\odot$  (assuming  $12 + \log(\text{O}/\text{H})_\odot = 8.69$ , see Asplund et al. 2009). If we adopt the mean oxygen abundance estimate  $12 + \log(\text{O}/\text{H}) = 8.18 \pm 0.09$  given by the PP04 and KK04 methods, the resulting metallicity becomes  $Z \simeq 0.3Z_\odot$  and agrees well with photoionization models. This is not surprising given that both methods have been calibrated by such models.

The  $[\text{S II}] \lambda 6717 + \lambda 6731/\text{H}\alpha$  line intensity ratio is a commonly used indicator of the shock excitation of gas. We tried to spectroscopically confirm the presence of the shock excitation mechanism in the eastern chain of H II regions, where Tonque & Westphal (1995) identified the synchrotron component of the radio emission, possibly indicative of the presence of supernova remnants. However, it is evident from Fig. 8 that the  $[\text{S II}] \lambda 6717 + \lambda 6731/\text{H}\alpha$  line intensity ratio does not exceed 0.2 in all regions, indicating the predominance of photoionization excitation in the areas considered. It is not surprising that no evidence for the shock excitation of gas could be found in the optical spectra. At the relative



**Figure 8.** Diagnostic diagrams based on the results of our observations of the Holmberg II galaxy and on the data of Croxall et al. (2009). Also shown are the theoretical photoionization models by Kewley et al. (2010) for different metallicities computed assuming the continuous star formation over 5 Myr. The dashed line in the upper panel the ratio  $I([\text{S II}] \lambda 6717 + \lambda 6731)/I(\text{H}\alpha) = 0.2$

distant galaxy the nebulae we analysed are large complexes of gas ionized by many stars, and optical emission of supernova remnants, if any, is hard to distinguish with the present spatial and spectral resolution. A detailed investigation of the kinematics of the nebulae by Fabry-Perot interferometer observations in  $\text{H}\alpha$  and  $[\text{S II}]$  lines that we defer to our forthcoming paper may be helpful in case we find evidence of supersonic gas velocities.

## 5 CONCLUSIONS.

We report relative oxygen, nitrogen, sulphur, neon, and argon abundance estimates in the Holmberg II galaxy based on the long-slit spectra taken at the 6-m telescope of the SAO RAS.

The oxygen, nitrogen, sulphur, argon and neon abundances in Holmberg II H II regions that we report in this paper are the most detailed estimates obtained for the galaxy used to date. According to our observations, the relative abundances of these elements in individual H II regions (excluding regions with high uncertainties) lie within the following intervals:  $12 + \log(\text{O}/\text{H}) = 7.38 - 7.89$  (or  $8.08 - 8.32$

depending on the method applied),  $12 + \log(\text{N}/\text{H}) = 5.92 - 6.51$ ,  $12 + \log(\text{S}/\text{H}) = 6.01 - 6.20$ ,  $12 + \log(\text{Ne}/\text{H}) = 6.89 - 7.07$ , and  $12 + \log(\text{Ar}/\text{H}) = 5.18 - 5.39$ . The average gas metallicity in the galaxy is  $Z \simeq 0.1 Z_{\odot}$  (if computed using the  $T_e$ , PT05, ONS, ON or NS method) or  $Z \simeq 0.3 Z_{\odot}$  (if computed using the PP04 or KK04 method).

We used our observations, which cover most of the H II regions in the galaxy, the data reported by Lee et al. (2003) and Croxall et al. (2009), as well as the results of our earlier observations of the Irr galaxy IC 10 and BCD galaxy VII Zw 403 to compare the currently most popular methods of the gas metallicity estimation in galaxies.

The results of this study, on the whole, confirm the conclusions of López-Sánchez et al. (2012) based on the analysis of ‘model’ H II regions. On the average, the estimates made using the so-called PT05, ON, NS, and ONS methods agree well with each other (although the ONS method yields overestimated abundances in some H II regions, compared to the results of other two methods). The PT05, ON, NS, and ONS methods yield lower metallicities compared to the ‘direct’  $T_e$  method. The PP04 and KK04 methods, which were used in this paper, on the contrary, yield systematically overestimated metallicities compared to the  $T_e$  method.

The PP04 method yields overestimated oxygen abundances for  $12 + \log(\text{O}/\text{H}) < 8.7$  that are similar to those obtained by the KK04 method, leading us to conclude that the two methods yield less reliable estimates for the objects considered than those given by the  $T_e$ , PT05, ON, NS and ONS methods.

We show the metallicity estimates based on the comparison of diagnostic diagrams with the photoionization models to be less reliable than those determined from bright oxygen lines.

We tried to confirm the supernova remnants in the eastern chain of H II regions suspected by Tonque & Westphal (1995). However, we did not find any excessive  $I([\text{S II}] \lambda 6717 + \lambda 6731)/I(\text{H}\beta)$  line intensity ratio that would be indicative of gas emission behind the shock.

The distributions of relative line intensities along the slits crossing the brightest and most extended H II regions proved to be non-uniform from the viewpoint of the structure and that of metallicity, temperature, and state of ionization. This fact may play a key part in the determination of metallicities of the entire regions and cause discrepancies between the estimates obtained using different methods.

We found a bright He II  $\lambda 4686$  line emission in the central part of the shell nebula HSK73. This emission may be indicative of the presence of a Wolf-Rayet star or another energetic source of intense UV emission.

We will study the structure and kinematics of the gas and dust structure of the Holmberg II in our forthcoming paper (Wiebe et al., in preparation).

## ACKNOWLEDGMENTS

This work was supported by the Russian Foundation for Basic Research (projects no. 10-02-00091 and 12-02-31356). O.V. Egorov acknowledges the support from the Dynasty Foundation of Non-commercial Programs and the Federal

Target Program ‘Research and Pedagogical Cadre for Innovative Russia’ (state contract no. 14.740.11.0800). This research was partly supported by the RAS program of the fundamental investigation OFN-17 ‘Active processes in galactic and extragalactic objects’.

We are grateful to Kevin Croxall for verifying and sharing the corrected spectrograph slit coordinates in the observations performed by his team, which we used in this work. Also we thank Vera Arkhipova for helpful discussions and Victor Afanasiev for his great contribution in the development of the spectroscopic technique at the 6-m telescope. We thank the anonymous referee for the constructive comments that improved the quality of the paper.

This work is based on the observations obtained with the 6-m telescope of the Special Astrophysical Observatory of the Russian Academy of Sciences. The observations were carried out with the financial support of the Ministry of Education and Science of Russian Federation (contracts no. 16.518.11.7073 and 14.518.11.7070). This research has made use of the NASA/IPAC Extragalactic Database (NED) which is operated by the Jet Propulsion Laboratory, California Institute of Technology, under contract with the National Aeronautics and Space Administration (USA).

## REFERENCES

- Afanasiev V.L., Moiseev A.V., 2005 *Astron. Letters*, 31, 194
- Afanasiev V.L., Moiseev A.V., 2011, *Baltic Astronomy*, 20, 363
- Arkhipova V.P., Lozinskaya T.A., Moiseev A.V., Egorov O.V., 2007, *Astron. Rep.*, 51, 871
- Arkhipova V.P., Egorov O.V., Lozinskaya T.A., Moiseev A.V., 2011, *Astron. Lett.*, 37, 65
- Asplund M., Grevesse N., Sauval A.J., Scott P., 2009, *ARA&A* 47, 481
- Bagetakos I., Brinks E., Walter F., de Blok W.J.G., Usero A., Leroy A.K., Rich J.W., Kennicutt R.C.Jr., 2011, *AJ*, 141, 23
- Braun R., Oosterloo T. A., Morganti R., Klein U., Beck R., 2007, *A&A*, 461, 455
- Cardelli, J.A., Clayton, G.C., Mathis, J.S., 1989, *ApJ*, 345, 245
- Cook D.O. et al., 2012, *ApJ*, 751, 100
- Croxall K.V., van Zee L., Lee H., Skillman E.D., Lee J.C., Côté S., Kennicutt R.C., Miller B.W., 2009, *ApJ*, 705, 723
- Egorov O.V., Lozinskaya T.A., 2011, *Ast. Bull.*, 66, 293
- Fitzpatrick E.L., 1999, *PASP*, 111, 63
- Garnett D.R., 1992, *AJ*, 103, 1330
- Hägele G.F., Díaz Á.I., Terlevich E., Terlevich R., Pérez-Montero E., Cardaci M.V., 2008, *MNRAS*, 383, 209
- Heald G., Braun R., Edmonds R., 2009, *A&A*, 503, 409
- Hodge P., Lee M.G., 1990, *PASP*, 102, 26
- Hodge P., Strobel N.V., Kennicutt R.C., 1994, *PASP*, 106, 309
- Hunter D.A., Hawley W.N., Gallagher J.S., 1993, *AJ*, 106, 1797
- Izotov Y.I., Stasińska G., Meynet G., Guseva N.G., Thuan T.X., 2006, *A&A*, 448, 955
- Karachentsev I.D. et al., 2003, *A&A*, 398, 479
- Karachentsev I.D., Kaisin S.S., 2007, *AJ*, 133, 1883
- Kennicutt R.C.Jr. et al., 2003, *PASP*, 115, 928
- Kewley L.J., Dopita M.A., 2002, *ApJS*, 142, 35
- Kewley L.J., Ellison S.L., 2008, *ApJ*, 681, 1183
- Kobulnicky H.A., Kewley L.J., 2004, *ApJ*, 617, 240
- Lee H., McCall M. L., Kingsburgh R. L., Ross R., Stevension C.C., 2003, *AJ*, 125, 146
- Lehmann I. et al., 2005, *A&A*, 431, 847
- Levesque E.M., Kewley L.J., Larson K.L., 2010, *AJ*, 139, 712
- López-Sánchez Á.R., Dopita M.A., Kewley L.J., Zahid H.J., Nicholls D.C., Scharwächter J., 2012, *MNRAS*, in press, astro-ph/1203.5021
- Lozinskaya T.A., Egorov O.V., Moiseev A.V., Bizyaev D.V., 2009, *Astron. Lett.*, 35, 730
- Masegosa J., Moles M., del Olmo A., 1991, *A&A*, 249, 505
- Moustakas J., Kennicutt R.C., Tremonti C.A., Dale D.A., Smith J.-D.T., Calzetti D., 2010, *ApJS*, 190, 233
- Osterbrock D.E., Ferland G.J., 2006, *Astrophysics of Gaseous Nebulae and Active Galactic Nuclei* (2nd ed.). Univ. Science Book, Sausalito, CA
- Pérez-Montero E., Díaz Á.I., 2003, *MNRAS*, 346, 105
- Pettini M., Pagel B., 2004, *MNRAS*, 348, L59
- Piembert M., 1967, *ApJ*, 150, 825
- Pilyugin L.S., Thuan T.X., 2005, *ApJ*, 631, 231
- Pilyugin L.S., Mattsson L., Vílchez J.M., Cedrés B., 2009, *MNRAS*, 398, 485
- Pilyugin L.S., Vílchez J.M., Thuan T.X., 2010, *ApJ*, 720, 1738
- Pilyugin L.S., Vílchez J.M., Mattsson L., Thuan T.X., 2012, *MNRAS*, 421, 1624
- Pilyugin L.S., Mattsson L., 2011, *MNRAS*, 412, 1145
- Schlegel D.J., Finkbeiner D.P., Davis M., 1998, *ApJ*, 500, 525
- Stasińska G., 1978, *A&A*, 66, 257
- Stasińska G., 1980, *A&A*, 84, 320
- Stasińska G., 1990, *A&AS*, 83, 501
- Stasińska G., 2005, *A&A*, 434, 507
- Stewart S.G. et al., 2000, *ApJ*, 529, 201
- Tongue T.D., Westphal D.J., 1995, *AJ*, 109, 2462
- Walter F. et al., 2007, *ApJ*, 661, 102
- Weisz D.R., Skillman E.D., Cannon J.M., Dolphin A.E., Kennicutt R.C.Jr., Lee J., Walter F., 2009, *ApJ*, 704, 1538

**Table 2.** Relative intensities of emission lines ( $I(\text{H}\beta)=100$ ).

HII region	HSK7	HSK15	HSK16	HSK17	HSK20	HSK25	HSK26	HSK31	HSK32	HSK41	HSK45
[O II] $\lambda 3727 + \lambda 3729$	—	—	—	—	—	—	—	—	924.2 $\pm$ 68.7	360.5 $\pm$ 6.9	217.6 $\pm$ 0.6
[Ne III] $\lambda 3869$	—	—	—	—	—	—	—	—	—	16.5 $\pm$ 4.2	26.8 $\pm$ 1.1
He I $\lambda 3970$	—	—	—	—	—	—	—	—	—	16.4 $\pm$ 3.1	21.6 $\pm$ 2.6
H $\delta$ $\lambda 4104$	20.5 $\pm$ 5.6	—	—	—	—	—	—	—	—	22.9 $\pm$ 0.9	24.0 $\pm$ 1.1
H $\gamma$ $\lambda 4340$	38.1 $\pm$ 0.9	51.1 $\pm$ 27.3	42.6 $\pm$ 6.0	38.7 $\pm$ 4.2	38.6 $\pm$ 14.5	—	—	40.6 $\pm$ 5.1	35.7 $\pm$ 18.3	47.5 $\pm$ 1.3	46.3 $\pm$ 1.6
[O III] $\lambda 4363$	8.5 $\pm$ 1.0	—	—	—	—	—	—	—	—	3.7 $\pm$ 0.6	6.5 $\pm$ 0.5
He I $\lambda 4471$	3.2 $\pm$ 0.7	—	—	—	—	—	—	—	—	3.0 $\pm$ 0.7	3.5 $\pm$ 0.2
He II $\lambda 4686$	—	—	—	—	—	—	—	—	—	—	—
He I $\lambda 4921$	—	—	—	—	—	—	—	—	—	0.86 $\pm$ 0.22	0.88 $\pm$ 0.47
[O III] $\lambda 5007$	425.4 $\pm$ 17.8	160.4 $\pm$ 8.4	205.9 $\pm$ 7.2	220.69 $\pm$ 16.9	101.4 $\pm$ 10.5	113.5 $\pm$ 2.2	48.5 $\pm$ 106.2	329.3 $\pm$ 4.1	86.3 $\pm$ 6.9	174.9 $\pm$ 2.0	357.8 $\pm$ 2.1
[O III] $\lambda 4959$	139.8 $\pm$ 6.8	53.0 $\pm$ 3.5	69.3 $\pm$ 3.0	74.4 $\pm$ 6.7	33.2 $\pm$ 4.2	35.4 $\pm$ 1.4	14.5 $\pm$ 41.0	109.0 $\pm$ 1.8	29.1 $\pm$ 3.0	58.5 $\pm$ 0.9	124.2 $\pm$ 0.9
He I $\lambda 5876$	11.0 $\pm$ 0.2	—	—	13.2 $\pm$ 1.3	15.1 $\pm$ 1.0	20.8 $\pm$ 0.7	—	22.9 $\pm$ 0.6	20.4 $\pm$ 1.8	10.9 $\pm$ 0.9	11.1 $\pm$ 0.5
[S III] $\lambda 6312$	1.6 $\pm$ 0.4	3.9 $\pm$ 0.8	2.6 $\pm$ 0.4	1.8 $\pm$ 1.0	2.1 $\pm$ 0.4	—	—	—	—	—	1.5 $\pm$ 0.1
[N II] $\lambda 6548$	2.0 $\pm$ 0.3	3.5 $\pm$ 1.9	2.8 $\pm$ 0.7	3.0 $\pm$ 0.3	3.6 $\pm$ 0.5	5.2 $\pm$ 0.6	9.6 $\pm$ 3.5	5.3 $\pm$ 3.6	4.1 $\pm$ 3.1	4.0 $\pm$ 0.6	3.0 $\pm$ 0.1
H $\alpha$ $\lambda 6563$	280.9 $\pm$ 7.4	249.0 $\pm$ 10.7	282.3 $\pm$ 6.9	279.6 $\pm$ 5.6	280.1 $\pm$ 9.6	279.8 $\pm$ 3.7	281.5 $\pm$ 8.9	280.5 $\pm$ 4.2	280.9 $\pm$ 22.0	280.9 $\pm$ 9.1	280.9 $\pm$ 13.6
[N II] $\lambda 6583$	3.7 $\pm$ 0.4	10.9 $\pm$ 4.7	9.1 $\pm$ 1.7	8.1 $\pm$ 0.5	11.3 $\pm$ 1.0	11.9 $\pm$ 0.5	19.8 $\pm$ 2.5	11.9 $\pm$ 6.4	12.1 $\pm$ 7.2	12.5 $\pm$ 1.4	8.2 $\pm$ 0.2
He I $\lambda 6678$	2.6 $\pm$ 0.1	—	—	2.4 $\pm$ 2.1	—	—	—	2.6 $\pm$ 0.8	—	2.5 $\pm$ 0.8	3.0 $\pm$ 0.1
[S II] $\lambda 6717$	7.0 $\pm$ 0.1	16.5 $\pm$ 2.3	20.0 $\pm$ 1.0	14.8 $\pm$ 0.4	30.1 $\pm$ 2.4	33.7 $\pm$ 1.3	39.3 $\pm$ 6.8	25.8 $\pm$ 1.3	33.7 $\pm$ 4.6	34.3 $\pm$ 1.0	17.8 $\pm$ 0.2
[S II] $\lambda 6731$	5.2 $\pm$ 0.1	11.4 $\pm$ 2.1	13.9 $\pm$ 1.0	10.9 $\pm$ 0.5	20.9 $\pm$ 2.1	23.8 $\pm$ 1.5	28.2 $\pm$ 6.9	18.4 $\pm$ 1.2	27.9 $\pm$ 5.1	24.2 $\pm$ 0.9	12.7 $\pm$ 0.2
He I $\lambda 7065$	—	—	—	1.5 $\pm$ 0.5	—	—	—	1.8 $\pm$ 0.4	—	2.2 $\pm$ 0.2	2.8 $\pm$ 0.2
[Ar III] $\lambda 7136$	4.6 $\pm$ 0.4	2.8 $\pm$ 1.6	4.1 $\pm$ 0.6	4.3 $\pm$ 2.4	2.5 $\pm$ 4.2	3.7 $\pm$ 0.6	—	7.0 $\pm$ 1.3	—	3.7 $\pm$ 0.7	5.5 $\pm$ 0.1
[O II] $\lambda 7320$	1.5 $\pm$ 0.1	—	3.6 $\pm$ 0.2	3.2 $\pm$ 0.2	4.3 $\pm$ 0.2	—	—	—	—	3.4 $\pm$ 0.2	2.8 $\pm$ 0.1
[O II] $\lambda 7330$	1.2 $\pm$ 0.1	—	2.8 $\pm$ 0.5	2.1 $\pm$ 0.3	2.9 $\pm$ 0.4	—	—	—	—	3.0 $\pm$ 0.4	2.2 $\pm$ 0.1

HII region	HSK56	HSK57	HSK59	HSK61	HSK65	HSK67	HSK69	HSK70	HSK71	HSK73 (PA187)	HSK73 (PA102)
[O II] $\lambda 3727 + \lambda 3729$	252.0 $\pm$ 8.2	—	267.5 $\pm$ 6.1	—	—	171.05 $\pm$ 4.1	272.1 $\pm$ 5.1	239.9 $\pm$ 6.7	205.6 $\pm$ 2.3	282.9 $\pm$ 2.4	204.1 $\pm$ 1.8
[Ne III] $\lambda 3869$	28.5 $\pm$ 8.4	—	14.4 $\pm$ 1.0	—	—	19.3 $\pm$ 4.3	7.5 $\pm$ 4.6	24.7 $\pm$ 2.1	21.9 $\pm$ 3.7	19.2 $\pm$ 5.0	23.0 $\pm$ 3.0
He I $\lambda 3970$	16.3 $\pm$ 10.6	—	14.8 $\pm$ 9.8	—	—	20.5 $\pm$ 0.3	16.7 $\pm$ 2.9	21.4 $\pm$ 8.6	21.0 $\pm$ 2.3	20.3 $\pm$ 6.0	20.1 $\pm$ 1.9
H $\delta$ $\lambda 4104$	20.3 $\pm$ 1.5	—	20.5 $\pm$ 0.5	—	—	23.9 $\pm$ 1.8	25.3 $\pm$ 1.7	24.7 $\pm$ 1.6	23.8 $\pm$ 0.9	24.9 $\pm$ 1.3	23.1 $\pm$ 1.0
H $\gamma$ $\lambda 4340$	47.4 $\pm$ 3.1	—	47.4 $\pm$ 1.7	31.6 $\pm$ 8.9	42.3 $\pm$ 47.3	45.9 $\pm$ 2.1	50.1 $\pm$ 3.7	47.5 $\pm$ 1.9	46.9 $\pm$ 2.3	49.1 $\pm$ 2.5	47.4 $\pm$ 1.3
[O III] $\lambda 4363$	5.9 $\pm$ 0.4	—	—	—	—	5.2 $\pm$ 1.4	1.5 $\pm$ 0.3	5.6 $\pm$ 0.7	5.7 $\pm$ 0.6	4.0 $\pm$ 3.5	6.3 $\pm$ 0.9
He I $\lambda 4471$	—	—	2.3 $\pm$ 3.4	—	—	3.5 $\pm$ 0.6	3.8 $\pm$ 0.8	3.3 $\pm$ 0.5	3.3 $\pm$ 0.3	5.4 $\pm$ 0.8	3.8 $\pm$ 0.2
He II $\lambda 4686$	—	—	—	—	—	—	—	1.8 $\pm$ 0.3	—	4.3 $\pm$ 1.1	—
He I $\lambda 4921$	2.71 $\pm$ 0.43	—	—	—	—	0.81 $\pm$ 0.72	—	—	0.69 $\pm$ 0.36	1.45 $\pm$ 0.62	1.37 $\pm$ 0.70
[O III] $\lambda 5007$	292.9 $\pm$ 1.9	90.6 $\pm$ 6.4	182.5 $\pm$ 1.9	206.1 $\pm$ 2.7	126.3 $\pm$ 2.2	297.1 $\pm$ 2.2	119.1 $\pm$ 2.5	293.4 $\pm$ 1.6	332.4 $\pm$ 3.8	223.1 $\pm$ 1.9	263.4 $\pm$ 2.1
[O III] $\lambda 4959$	98.7 $\pm$ 0.8	40.2 $\pm$ 5.6	61.2 $\pm$ 0.8	67.7 $\pm$ 1.8	42.1 $\pm$ 1.1	99.3 $\pm$ 0.9	39.4 $\pm$ 1.0	97.9 $\pm$ 0.7	107.6 $\pm$ 1.5	73.0 $\pm$ 0.8	89.2 $\pm$ 0.9
He I $\lambda 5876$	13.1 $\pm$ 0.8	93.0 $\pm$ 1.9	9.8 $\pm$ 1.5	33.5 $\pm$ 0.9	20.1 $\pm$ 1.0	10.1 $\pm$ 0.3	13.4 $\pm$ 1.5	9.7 $\pm$ 1.0	10.4 $\pm$ 1.3	14.2 $\pm$ 1.1	11.4 $\pm$ 0.8
[S III] $\lambda 6312$	—	—	—	—	5.8 $\pm$ 4.9	1.6 $\pm$ 1.3	—	1.3 $\pm$ 0.2	1.2 $\pm$ 0.1	1.8 $\pm$ 2.0	—
[N II] $\lambda 6548$	2.7 $\pm$ 0.9	9.5 $\pm$ 2.6	2.1 $\pm$ 0.3	3.7 $\pm$ 0.9	2.0 $\pm$ 0.3	1.7 $\pm$ 0.2	4.0 $\pm$ 2.0	2.0 $\pm$ 0.2	2.6 $\pm$ 0.2	3.9 $\pm$ 0.3	2.2 $\pm$ 0.2
H $\alpha$ $\lambda 6563$	280.9 $\pm$ 10.7	279.5 $\pm$ 25.3	280.9 $\pm$ 9.6	282.4 $\pm$ 12.4	279.7 $\pm$ 4.3	275.7 $\pm$ 8.0	335.3 $\pm$ 9.1	280.5 $\pm$ 3.4	279.5 $\pm$ 6.6	293.7 $\pm$ 3.7	280.9 $\pm$ 10.0
[N II] $\lambda 6583$	8.7 $\pm$ 2.1	13.6 $\pm$ 1.3	8.9 $\pm$ 1.0	7.5 $\pm$ 0.7	6.5 $\pm$ 0.4	3.9 $\pm$ 0.3	6.4 $\pm$ 1.7	6.1 $\pm$ 0.4	5.9 $\pm$ 0.2	8.5 $\pm$ 0.5	6.4 $\pm$ 0.4
He I $\lambda 6678$	—	—	—	—	2.4 $\pm$ 0.5	2.5 $\pm$ 1.4	—	2.3 $\pm$ 0.2	2.7 $\pm$ 0.6	4.1 $\pm$ 1.5	2.3 $\pm$ 0.3
[S II] $\lambda 6717$	23.6 $\pm$ 1.3	27.9 $\pm$ 30.2	21.3 $\pm$ 1.3	17.3 $\pm$ 12.0	19.7 $\pm$ 0.6	8.3 $\pm$ 0.3	19.0 $\pm$ 1.8	15.6 $\pm$ 0.4	11.0 $\pm$ 0.2	18.8 $\pm$ 1.1	19.0 $\pm$ 0.4
[S II] $\lambda 6731$	14.9 $\pm$ 1.0	21.4 $\pm$ 29.6	15.1 $\pm$ 1.2	13.1 $\pm$ 11.5	14.4 $\pm$ 0.9	5.8 $\pm$ 0.3	12.9 $\pm$ 2.0	10.7 $\pm$ 0.4	8.0 $\pm$ 0.2	13.0 $\pm$ 0.9	12.8 $\pm$ 0.3
He I $\lambda 7065$	—	—	—	—	1.3 $\pm$ 0.5	2.0 $\pm$ 0.7	—	1.6 $\pm$ 0.3	2.5 $\pm$ 0.9	4.1 $\pm$ 1.3	—
[Ar III] $\lambda 7136$	4.5 $\pm$ 1.4	—	3.6 $\pm$ 0.4	4.6 $\pm$ 1.0	3.5 $\pm$ 0.6	3.9 $\pm$ 0.4	—	3.7 $\pm$ 0.4	4.5 $\pm$ 0.9	4.6 $\pm$ 3.3	3.8 $\pm$ 0.6
[O II] $\lambda 7320$	—	—	6.9 $\pm$ 0.3	—	—	1.9 $\pm$ 0.1	—	2.1 $\pm$ 0.1	2.3 $\pm$ 2.1	2.7 $\pm$ 0.2	3.4 $\pm$ 0.1
[O II] $\lambda 7330$	—	—	5.3 $\pm$ 0.6	—	—	1.5 $\pm$ 0.2	—	1.6 $\pm$ 0.3	1.9 $\pm$ 2.3	2.3 $\pm$ 0.4	1.6 $\pm$ 0.1

**Table 3.** Physical properties of ionized gas and elemental abundances in H II regions

HII region reference	HSK7 PA347	HSK15 PA347	HSK16 PA347	HSK17 PA347	HSK20 PA347	HSK25 PA304	HSK26 PA347	HSK31 PA304	HSK32 PA102	HSK41 PA102	HSK41 Cr8	HSK45 PA102
$E(B - V)$ , mag	0.19 ± 0.04	—	0.10 ± 0.03	0.25 ± 0.03	0.19 ± 0.05	0.34 ± 0.11	0.13 ± 0.03	0.16 ± 0.02	0.41 ± 0.10	0.15 ± 0.06	—	0.18 ± 0.06
$n_e$ , cm <sup>-3</sup>	80 ± 10	—	10 ± 40	70 ± 30	10 ± 80	20 ± 40	40 ± 190	40 ± 50	220 ± 200	20 ± 30	180 ± 140	30 ± 10
$T_e$ ([O III]), K	15200 ± 900	—	—	—	—	—	—	—	—	15600 ± 1100	—	14600 ± 400
$T_e$ ([O II]), K	12300 ± 600	—	—	—	—	—	—	—	—	12200 ± 700	—	12200 ± 300
$T_e$ ([S III]), K	15400 ± 1100	—	—	—	—	—	—	—	—	15100 ± 1100	—	14700 ± 500
12 + log (O <sup>+</sup> /H <sup>+</sup> )	—	—	—	—	—	—	—	—	—	7.75 ± 0.08	—	7.53 ± 0.03
12 + log (O <sup>2+</sup> /H <sup>+</sup> )	7.66 ± 0.06	—	—	—	—	—	—	—	—	7.25 ± 0.07	—	7.64 ± 0.03
12 + log (O/H) (T <sub>e</sub> )	—	—	—	—	—	—	—	—	—	7.87 ± 0.07	—	7.89 ± 0.02
12 + log (O/H) (PT05)	—	—	—	—	—	—	—	—	—	—	—	7.90 ± 0.01
12 + log (O/H) (ONS)	—	—	—	—	—	—	—	—	7.71 ± 0.08	7.91 ± 0.01	7.88 ± 0.04	7.83 ± 0.01
12 + log (O/H) (ON)	—	—	—	—	—	—	—	—	7.33 ± 0.16	7.68 ± 0.03	7.71 ± 0.04	7.87 ± 0.01
12 + log (O/H) (NS)	7.76 ± 0.03	7.63 ± 0.10	7.68 ± 0.05	7.69 ± 0.03	7.45 ± 0.04	7.53 ± 0.02	7.34 ± 0.73	7.97 ± 0.12	7.41 ± 0.14	7.70 ± 0.03	7.72 ± 0.03	7.89 ± 0.02
12 + log (O/H) (PP04)	—	8.23 ± 0.06	8.15 ± 0.03	8.13 ± 0.01	8.28 ± 0.02	8.27 ± 0.01	8.46 ± 0.30	8.12 ± 0.07	8.31 ± 0.08	8.22 ± 0.02	8.23 ± 0.02	—
12 + log (O/H) (KK04)	—	—	—	—	—	—	—	—	—	8.26 ± 0.09	8.16 ± 0.27	8.23 ± 0.04
12 + log (N <sup>+</sup> /H <sup>+</sup> )	5.66 ± 0.06	—	—	—	—	—	—	—	—	6.12 ± 0.06	—	5.95 ± 0.02
12 + log (N/H) (T <sub>e</sub> )	6.29 ± 0.07	—	—	—	—	—	—	—	—	6.29 ± 0.07	—	6.36 ± 0.03
12 + log (N/H) (ONS)	—	—	—	—	—	—	—	—	5.78 ± 0.27	6.31 ± 0.05	6.40 ± 0.06	6.36 ± 0.01
12 + log (N/H) (ON)	—	—	—	—	—	—	—	—	5.46 ± 0.23	6.13 ± 0.04	6.28 ± 0.05	6.36 ± 0.01
12 + log (N/H) (NS)	6.32 ± 0.03	6.23 ± 0.12	6.21 ± 0.09	6.25 ± 0.03	5.96 ± 0.08	6.05 ± 0.02	5.93 ± 0.70	6.51 ± 0.14	5.92 ± 0.16	6.20 ± 0.03	6.25 ± 0.03	6.41 ± 0.01
log (N/O) (T <sub>e</sub> )	—	—	—	—	—	—	—	—	—	-1.63 ± 0.10	—	-1.56 ± 0.03
log (N/O) (ONS)	—	—	—	—	—	—	—	—	-1.93 ± 0.28	-1.60 ± 0.05	-1.48 ± 0.08	-1.47 ± 0.01
log (N/O) (ON)	—	—	—	—	—	—	—	—	-1.87 ± 0.28	-1.55 ± 0.05	-1.44 ± 0.06	-1.51 ± 0.01
log (N/O) (NS)	-1.44 ± 0.04	-1.41 ± 0.16	-1.47 ± 0.07	-1.44 ± 0.04	-1.48 ± 0.06	-1.48 ± 0.02	-1.41 ± 1.01	-1.46 ± 0.19	-1.50 ± 0.21	-1.50 ± 0.04	-1.48 ± 0.04	-1.47 ± 0.01
12 + log (S <sup>+</sup> /H <sup>+</sup> )	5.24 ± 0.04	—	—	—	—	—	—	—	—	5.92 ± 0.05	—	5.64 ± 0.02
12 + log (S <sup>2+</sup> /H <sup>+</sup> )	5.88 ± 0.13	—	—	—	—	—	—	—	—	—	—	5.91 ± 0.06
12 + log (S/H)	6.03 ± 0.11	—	—	—	—	—	—	—	—	—	—	6.11 ± 0.04
12 + log (Ar <sup>2+</sup> /H <sup>+</sup> )	5.25 ± 0.06	—	—	—	—	—	—	—	—	5.17 ± 0.09	—	5.36 ± 0.03
12 + log (Ar/H)	5.28 ± 0.06	—	—	—	—	—	—	—	—	5.23 ± 0.10	—	5.39 ± 0.03
12 + log (Ne <sup>+</sup> /H <sup>+</sup> )	6.98 ± 0.75	—	—	—	—	—	—	—	—	6.60 ± 0.14	—	6.89 ± 0.04
12 + log (Ne/H)	7.04 ± 0.75	—	—	—	—	—	—	—	—	6.93 ± 0.14	—	7.05 ± 0.04

HII region reference	HSK45 Cr7	HSK45 Cr9	HSK50 Cr5	HSK56 PA102	HSK57 PA304	HSK59 PA102	HSK61 PA304	HSK65 PA304	HSK67 PA187	HSK67 Cr13	HSK67 Lee	HSK69 PA187
$E(B - V)$ , mag	—	—	—	0.15 ± 0.14	0.12 ± 0.12	0.10 ± 0.08	0.07 ± 0.06	0.06 ± 0.02	0.09 ± 0.07	—	—	0.15 ± 0.10
$n_e$ , cm <sup>-3</sup>	70 ± 100	40 ± 100	110 ± 120	—	120 ± 1320	20 ± 60	100 ± 820	60 ± 30	20 ± 40	—	—	—
$T_e$ ([O III]), K	13300 ± 600	14500 ± 1200	13400 ± 800	15200 ± 400	—	—	—	—	14300 ± 1500	13300 ± 500	22600 ± 5700	12600 ± 1100
$T_e$ ([O II]), K	11800 ± 400	12200 ± 800	11900 ± 600	12300 ± 300	—	—	—	—	12200 ± 1100	11900 ± 400	—	11500 ± 800
$T_e$ ([S III]), K	13500 ± 800	14700 ± 1500	13600 ± 1100	14800 ± 400	—	—	—	—	14100 ± 1700	13300 ± 400	20200 ± 2400	12200 ± 1400
12 + log (O <sup>+</sup> /H <sup>+</sup> )	7.46 ± 0.06	7.56 ± 0.11	7.54 ± 0.08	7.59 ± 0.04	—	—	—	—	7.43 ± 0.13	7.13 ± 0.05	—	7.72 ± 0.11
12 + log (O <sup>2+</sup> /H <sup>+</sup> )	7.75 ± 0.05	7.61 ± 0.09	7.72 ± 0.07	7.50 ± 0.03	—	—	—	—	7.57 ± 0.12	7.72 ± 0.04	6.96 ± 0.21	7.33 ± 0.10
12 + log (O/H) (T <sub>e</sub> )	7.93 ± 0.04	7.89 ± 0.07	7.94 ± 0.05	7.85 ± 0.02	—	—	—	—	7.81 ± 0.09	7.82 ± 0.04	—	7.87 ± 0.09
12 + log (O/H) (PT05)	7.76 ± 0.02	7.91 ± 0.03	7.84 ± 0.03	7.89 ± 0.01	—	—	—	—	7.71 ± 0.01	7.47 ± 0.02	—	—
12 + log (O/H) (ONS)	7.80 ± 0.03	7.82 ± 0.04	7.72 ± 0.04	7.84 ± 0.03	—	7.74 ± 0.02	—	—	7.55 ± 0.01	7.47 ± 0.03	—	7.63 ± 0.04
12 + log (O/H) (ON)	7.89 ± 0.03	7.85 ± 0.03	7.74 ± 0.04	7.78 ± 0.07	—	7.58 ± 0.03	—	—	7.58 ± 0.03	7.57 ± 0.03	—	7.39 ± 0.08
12 + log (O/H) (NS)	7.89 ± 0.02	7.87 ± 0.02	7.77 ± 0.03	7.80 ± 0.06	7.57 ± 0.05	7.60 ± 0.03	7.66 ± 0.03	7.38 ± 0.02	7.61 ± 0.02	7.57 ± 0.02	—	7.42 ± 0.07
12 + log (O/H) (PP04)	—	—	—	—	8.32 ± 0.02	8.17 ± 0.02	8.13 ± 0.01	8.18 ± 0.01	—	—	—	8.16 ± 0.04
12 + log (O/H) (KK04)	8.15 ± 0.38	8.23 ± 0.39	8.19 ± 0.38	8.21 ± 0.11	—	8.13 ± 0.06	—	—	8.09 ± 0.06	7.94 ± 0.38	8.13 ± 0.49	8.08 ± 0.06
12 + log (N <sup>+</sup> /H <sup>+</sup> )	5.99 ± 0.04	5.98 ± 0.07	5.83 ± 0.06	5.96 ± 0.09	—	—	—	—	5.65 ± 0.09	5.53 ± 0.04	—	5.98 ± 0.13
12 + log (N/H) (T <sub>e</sub> )	6.49 ± 0.05	6.35 ± 0.08	6.27 ± 0.07	6.26 ± 0.09	—	—	—	—	6.08 ± 0.11	6.19 ± 0.05	—	6.17 ± 0.13
12 + log (N/H) (ONS)	6.44 ± 0.05	6.35 ± 0.05	6.17 ± 0.06	6.28 ± 0.11	—	6.15 ± 0.05	—	—	5.98 ± 0.04	6.07 ± 0.05	—	6.02 ± 0.14
12 + log (N/H) (ON)	6.49 ± 0.03	6.34 ± 0.04	6.15 ± 0.05	6.23 ± 0.10	—	6.02 ± 0.05	—	—	5.95 ± 0.03	6.11 ± 0.04	—	5.82 ± 0.12
12 + log (N/H) (NS)	6.42 ± 0.02	6.42 ± 0.02	6.29 ± 0.03	6.30 ± 0.07	6.16 ± 0.15	6.12 ± 0.03	6.20 ± 0.09	5.87 ± 0.02	6.15 ± 0.02	6.09 ± 0.03	—	5.94 ± 0.08
log (N/O) (T <sub>e</sub> )	-1.46 ± 0.06	-1.57 ± 0.11	-1.70 ± 0.08	-1.62 ± 0.09	—	—	—	—	-1.75 ± 0.14	-1.63 ± 0.06	—	-1.74 ± 0.16
log (N/O) (ONS)	-1.37 ± 0.06	-1.47 ± 0.07	-1.54 ± 0.07	-1.55 ± 0.11	—	-1.59 ± 0.06	—	—	-1.57 ± 0.04	-1.40 ± 0.06	—	-1.61 ± 0.14
log (N/O) (ON)	-1.40 ± 0.04	-1.51 ± 0.05	-1.58 ± 0.06	-1.55 ± 0.12	—	-1.57 ± 0.06	—	—	-1.63 ± 0.04	-1.46 ± 0.05	—	-1.58 ± 0.14
log (N/O) (NS)	-1.47 ± 0.03	-1.45 ± 0.03	-1.48 ± 0.04	-1.50 ± 0.09	-1.41 ± 0.15	-1.49 ± 0.04	-1.46 ± 0.10	-1.51 ± 0.03	-1.46 ± 0.03	-1.47 ± 0.04	—	-1.47 ± 0.11
12 + log (S <sup>+</sup> /H <sup>+</sup> )	5.66 ± 0.04	5.61 ± 0.06	5.53 ± 0.05	5.73 ± 0.03	—	—	—	—	5.31 ± 0.08	5.19 ± 0.03	—	5.71 ± 0.07
12 + log (S <sup>2+</sup> /H <sup>+</sup> )	6.06 ± 0.10	5.97 ± 0.17	6.15 ± 0.15	—	—	—	—	—	5.99 ± 0.41	5.88 ± 0.11	—	—
12 + log (S/H)	6.24 ± 0.07	6.14 ± 0.12	6.26 ± 0.12	—	—	—	—	—	6.09 ± 0.34	6.04 ± 0.09	—	—
12 + log (Ar <sup>2+</sup> /H <sup>+</sup> )	5.48 ± 0.06	5.30 ± 0.09	5.47 ± 0.08	5.27 ± 0.14	—	—	—	—	5.25 ± 0.10	5.28 ± 0.05	—	—
12 + log (Ar/H)	5.51 ± 0.06	5.34 ± 0.09	5.51 ± 0.08	5.31 ± 0.14	—	—	—	—	5.28 ± 0.10	5.32 ± 0.05	—	—
12 + log (Ne <sup>+</sup> /H <sup>+</sup> )	7.00 ± 0.06	—	—	6.86 ± 0.13	—	—	—	—	6.77 ± 0.17	6.80 ± 0.05	6.52 ± 0.24	6.54 ± 0.29
12 + log (Ne/H)	7.12 ± 0.06	—	—	7.07 ± 0.13	—	—	—	—	6.89 ± 0.17	6.86 ± 0.05	6.64 ± 0.24	6.88 ± 0.29



**Table 3.** Continued.

HII region reference	HSK69 Lee	HSK70 PA187	HSK70 Lee	HSK70 Cr11	HSK71 PA187	HSK71 Lee	HSK73 PA187	HSK73 PA102	HSK73 Lee	HSK73 Cr4	HSK74 Cr3	HSK82 Cr2
$E(B - V)$ , mag	—	0.21 ± 0.09	—	—	0.27 ± 0.08	—	0.16 ± 0.09	0.16 ± 0.06	—	—	—	—
$n_e$ , cm <sup>-3</sup>	—	—	—	50 ± 90	40 ± 20	—	—	—	—	40 ± 110	60 ± 100	10 ± 120
$T_e([O\ III])$ , K	17400 ± 8100	14800 ± 800	15900 ± 1600	15600 ± 1000	14200 ± 600	14800 ± 1400	14500 ± 3400	16600 ± 1100	13400 ± 2700	13400 ± 1000	14000 ± 400	12500 ± 1000
$T_e([O\ II])$ , K	11000 ± 3600	12300 ± 500	12100 ± 900	12200 ± 700	12200 ± 400	12200 ± 900	12200 ± 2400	11800 ± 600	11900 ± 2000	11900 ± 700	12100 ± 300	11500 ± 800
$T_e([S\ III])$ , K	16800 ± 7000	14500 ± 800	15500 ± 1500	15200 ± 1000	14300 ± 700	14400 ± 1400	14100 ± 3600	16100 ± 900	13200 ± 3400	13300 ± 1300	14400 ± 600	12600 ± 1500
12 + log (O <sup>+</sup> /H <sup>+</sup> )	7.76 ± 0.56	7.57 ± 0.06	7.48 ± 0.12	7.44 ± 0.08	7.51 ± 0.05	7.35 ± 0.12	7.64 ± 0.30	7.56 ± 0.07	7.60 ± 0.27	7.51 ± 0.10	7.10 ± 0.04	7.14 ± 0.11
12 + log (O <sup>2+</sup> /H <sup>+</sup> )	7.02 ± 0.46	7.53 ± 0.05	7.41 ± 0.11	7.50 ± 0.07	7.63 ± 0.04	7.54 ± 0.10	7.43 ± 0.26	7.36 ± 0.06	7.50 ± 0.23	7.62 ± 0.08	7.75 ± 0.03	7.86 ± 0.09
12 + log (O/H) (T <sub>e</sub> )	7.83 ± 0.48	7.85 ± 0.04	7.75 ± 0.08	7.77 ± 0.05	7.87 ± 0.03	7.76 ± 0.08	7.85 ± 0.21	7.78 ± 0.05	7.86 ± 0.18	7.87 ± 0.06	7.84 ± 0.03	7.93 ± 0.08
12 + log (O/H) (PT05)	—	7.87 ± 0.01	7.72 ± 0.05	7.74 ± 0.02	7.83 ± 0.01	7.63 ± 0.05	—	7.75 ± 0.01	—	7.72 ± 0.02	7.57 ± 0.02	7.51 ± 0.02
12 + log (O/H) (ONS)	—	7.74 ± 0.01	—	7.78 ± 0.03	7.69 ± 0.01	—	7.79 ± 0.01	7.72 ± 0.01	—	7.71 ± 0.04	7.61 ± 0.03	7.67 ± 0.03
12 + log (O/H) (ON)	—	7.69 ± 0.02	—	7.83 ± 0.03	7.74 ± 0.01	—	7.69 ± 0.02	7.66 ± 0.02	—	7.72 ± 0.04	7.66 ± 0.04	7.78 ± 0.04
12 + log (O/H) (NS)	—	7.72 ± 0.01	—	7.83 ± 0.02	7.77 ± 0.01	—	7.72 ± 0.01	7.68 ± 0.02	—	7.73 ± 0.03	7.66 ± 0.03	7.76 ± 0.03
12 + log (O/H) (PP04)	—	—	—	—	—	—	8.13 ± 0.01	—	—	—	—	—
12 + log (O/H) (KK04)	8.05 ± 0.42	8.20 ± 0.08	8.09 ± 0.53	8.12 ± 0.33	8.18 ± 0.07	8.04 ± 0.60	8.19 ± 0.04	8.11 ± 0.04	8.11 ± 0.43	8.09 ± 0.31	8.03 ± 0.45	7.99 ± 0.50
12 + log (N <sup>+</sup> /H <sup>+</sup> )	—	5.83 ± 0.04	—	5.96 ± 0.05	5.84 ± 0.03	—	6.00 ± 0.18	5.88 ± 0.05	—	5.91 ± 0.07	5.52 ± 0.04	5.76 ± 0.08
12 + log (N/H) (T <sub>e</sub> )	—	6.19 ± 0.05	—	6.32 ± 0.06	6.25 ± 0.04	—	6.27 ± 0.22	6.12 ± 0.06	—	6.31 ± 0.08	6.22 ± 0.05	6.52 ± 0.10
12 + log (N/H) (ONS)	—	6.13 ± 0.03	—	6.37 ± 0.05	6.19 ± 0.02	—	6.24 ± 0.03	6.15 ± 0.03	—	6.23 ± 0.06	6.17 ± 0.06	6.43 ± 0.07
12 + log (N/H) (ON)	—	6.06 ± 0.03	—	6.40 ± 0.03	6.17 ± 0.02	—	6.13 ± 0.02	6.10 ± 0.03	—	6.23 ± 0.05	6.20 ± 0.05	6.50 ± 0.06
12 + log (N/H) (NS)	—	6.23 ± 0.02	—	6.35 ± 0.02	6.33 ± 0.01	—	6.26 ± 0.02	6.17 ± 0.02	—	6.25 ± 0.03	6.14 ± 0.03	6.30 ± 0.04
log (N/O) (T <sub>e</sub> )	—	-1.69 ± 0.07	—	-1.48 ± 0.08	-1.65 ± 0.05	—	-1.62 ± 0.31	-1.70 ± 0.08	—	-1.58 ± 0.10	-1.62 ± 0.06	-1.42 ± 0.13
log (N/O) (ONS)	—	-1.61 ± 0.03	—	-1.41 ± 0.06	-1.50 ± 0.02	—	-1.54 ± 0.03	-1.57 ± 0.03	—	-1.48 ± 0.07	-1.44 ± 0.07	-1.24 ± 0.08
log (N/O) (ON)	—	-1.62 ± 0.03	—	-1.42 ± 0.05	-1.57 ± 0.02	—	-1.56 ± 0.03	-1.56 ± 0.03	—	-1.49 ± 0.06	-1.46 ± 0.06	-1.29 ± 0.07
log (N/O) (NS)	—	-1.49 ± 0.02	—	-1.48 ± 0.03	-1.44 ± 0.02	—	-1.46 ± 0.02	-1.52 ± 0.02	—	-1.48 ± 0.04	-1.52 ± 0.04	-1.46 ± 0.05
12 + log (S <sup>+</sup> /H <sup>+</sup> )	—	5.57 ± 0.04	—	5.68 ± 0.05	5.44 ± 0.03	—	5.65 ± 0.17	5.69 ± 0.04	—	5.64 ± 0.06	5.30 ± 0.03	5.39 ± 0.07
12 + log (S <sup>2+</sup> /H <sup>+</sup> )	—	5.87 ± 0.09	—	5.80 ± 0.11	5.85 ± 0.08	—	6.05 ± 0.59	—	—	—	6.02 ± 0.07	6.19 ± 0.20
12 + log (S/H)	—	6.06 ± 0.06	—	6.06 ± 0.06	6.01 ± 0.05	—	6.20 ± 0.42	—	—	—	6.20 ± 0.06	6.39 ± 0.18
12 + log (Ar <sup>2+</sup> /H <sup>+</sup> )	—	5.19 ± 0.06	—	5.10 ± 0.06	5.29 ± 0.10	—	5.31 ± 0.37	5.13 ± 0.08	—	5.25 ± 0.10	5.32 ± 0.05	5.45 ± 0.11
12 + log (Ar/H)	—	5.23 ± 0.06	—	5.13 ± 0.06	5.33 ± 0.10	—	5.36 ± 0.37	5.18 ± 0.08	—	5.29 ± 0.10	5.36 ± 0.05	5.50 ± 0.11
12 + log (Ne <sup>+</sup> /H <sup>+</sup> )	—	6.83 ± 0.07	6.77 ± 0.12	6.61 ± 0.08	6.84 ± 0.09	6.72 ± 0.13	6.75 ± 0.32	6.66 ± 0.09	6.93 ± 0.28	—	6.92 ± 0.04	—
12 + log (Ne/H)	—	6.99 ± 0.07	6.94 ± 0.13	6.76 ± 0.08	6.98 ± 0.09	6.83 ± 0.13	6.97 ± 0.33	6.89 ± 0.09	7.15 ± 0.29	—	6.97 ± 0.04	—

Note. References PA102, PA187, PA304 and PA331 denote our observational data according to position angle of the slit. Reference ‘Lee’ denotes regions investigated using Lee et al. (2003) observational data. References ‘Cr’ mark regions investigated using Croxall et al. (2009) observational data according to slit names in paper above.